Article

Metabolic support protects mucosa from ferroptosis in radiation-induced mucositis

Weiwei Yu[1,8], Kai Jiao [2,8], Kaiyan Wang[1,8], Xiang Li[1,8], Qianqian Wan [1], Wen Qin[1], Xinyi Hao[1], Meichen Wan[1], Yuxuan Ma[1], Jiao Wu [3], Qing Liu[1], Mei Shi[4], Conrado Aparicio [5,6], Franklin Tay[7] & Lina Niu [1]✉

Ionizing radiation is effective in treating cancer but causes significant damage to the mucosa, thereby increasing patient discomfort, delaying therapy, and raising the risk of mortality. The underlying mechanisms of this damage remain poorly understood, and current treatments are largely palliative. In this study, ferroptosis was identified as the primary mode of cell death responsible for the radiation-induced depletion of oral mucosal epithelial cells. Notably, a compensatory phase was also discovered in the early stages following radiation exposure, during which fibroblasts provide crucial metabolic support. Specifically, fibroblasts supply polyamines that are readily absorbed by basal epithelial cells, protecting them from ferroptosis. Supplementation with polyamines was found to effectively prevent mucosal injury. These findings highlight the critical role of fibroblast-mediated metabolic support in protecting the oral mucosa from radiation-induced damage and offer insights into enhancing the body's intrinsic protective mechanisms against radiation-related diseases.

Radiotherapy, though effective in eliminating tumors, often results in mucosal damage across the gastrointestinal tract, respiratory tract, and oral cavity. This damage significantly reduces patients' quality of life and may lead to treatment interruptions or increased mortality risk[1–3]. Among these complications, radiation-induced oral mucositis (RIOM) has emerged as a classic model for investigating the mechanisms and prevention of radiation-related mucosal injuries, owing to its high incidence, ease of clinical follow-up, and well-established animal models[3]. RIOM is typically characterized by mucosal atrophy or ulceration, accompanied by severe pain and compromised barrier function. These symptoms arise primarily from the death of epithelial cells following exposure to ionizing radiation[4–6].

Previous studies indicate that ionizing radiation directly induces DNA double-strand breaks and generates reactive oxygen species (ROS), which in turn damage critical biomolecules[7]. These injuries lead to the upregulation of apoptosis-related cytokines and the activation of downstream signaling pathways, ultimately contributing to mucosal barrier disruption[3,4]. However, the limited clinical efficacy of anti-apoptotic agents in treating RIOM[5–7] suggests that other forms of cell death may be involved in disease progression. Consequently, further exploration of the mechanisms of epithelial cell death may offer novel insights into preserving mucosal structure and function during radiotherapy, thereby improving clinical outcomes.

[1]State Key Laboratory of Oral & Maxillofacial Reconstruction and Regeneration, National Clinical Research Center for Oral Diseases, School of Stomatology, The Fourth Military Medical University, Xi'an, Shaanxi, China. [2]Department of Stomatology, Tangdu hospital, The Fourth Military Medical University, Xi'an, Shaanxi, China. [3]Department of Cell Biology, National Translational Science Center for Molecular Medicine, The Fourth Military Medical University, Xi'an, Shaanxi, China. [4]Department of Radiotherapy, Xijing Hospital, The Fourth Military Medical University, Xi'an, Shaanxi, China. [5]Catalan Institute for Research and Advanced Studies (ICREA), Passeig Luís Companys 23, Barcelona, Spain. [6]BOBl-Bioinspired Oral Biomaterials and Interfaces, Department of Materials Science and Engineering, Barceloa East School of Engineering (EEBE), Universitat Politècnica de Catalunya-Barcelona Tech (UPC), C/. Eduard Maristany 16, Barcelona, Spain. [7]The Dental College of Georgia, Augusta University, Augusta, GA, USA. [8]These authors contributed equally: Weiwei Yu, Kai Jiao, Kaiyan Wang, Xiang Li. ✉e-mail: niulina831013@126.com

In this study, we employed single-cell RNA sequencing (scRNA-seq) and confirmed that ferroptosis is the primary mode of epithelial cell death induced by radiation. Currently, ferroptosis is mainly inhibited by halting the propagation of lipid peroxyl radicals and chelating intracellular iron[8,9]. We found that treatment with Liproxstatin-1 (LIP-1), a specific ferroptosis inhibitor, effectively suppresses radiation-induced epithelial cell death and alleviates mucosal damage. However, due to potential safety concerns, this approach may not represent an optimal long-term strategy for treating RIOM[10–12]. Therefore, a deeper understanding of ferroptosis in epithelial cells is essential for developing alternative therapeutic approaches.

Interestingly, in the early stages following radiation exposure, we observed that epithelial cell death was not significant, with even an increase in the thickness of the oral mucosa. This finding suggests that the body may enter a compensatory and adaptive phase in response to radiation stress. Based on this observation, we propose that enhancing this intrinsic early-stage protective mechanism could help maintain epithelial cell integrity and prevent cell death in the later stages of radiation exposure.

The objective of this study was to elucidate the mechanisms underlying mucosal damage in RIOM by identifying the specific modes of epithelial cell death triggered by ionizing radiation. We discovered that, shortly after radiation, intercellular communication within the mucosal microenvironment provides critical metabolic support for epithelial cell survival. Moreover, supplementing such metabolic support can effectively prevent RIOM. These findings highlight a self-protective mechanism employed by the body under radiation stress and suggest that enhancing this intercellular communication could offer a promising strategy for preventing radiation-induced diseases and improving radiotherapy outcomes.

Results

The effect of ionizing radiation on epithelial homeostasis

The impact of radiation on the oral mucosa was examined using biopsies from human tongues affected by RIOM (Fig. 1a). Significant epithelial thinning and discontinuity were observed, along with reduced basal cell proliferation (Fig. 1b-d and Supplementary Fig. 1a-c). For in vivo modeling, C57BL/6 mice were exposed to 18 Gy cranial radiation. Oral mucosa damage appeared on day 9 post-radiation (Fig. 1e). Histological analysis revealed mucositis manifestations in the murine specimens that closely resembled those observed in the human tongue tissues (Fig. 1f, g). Suppressed basal cell proliferation was also evident (Fig. 1h).

To investigate cellular changes, scRNA-seq was performed on murine tongue mucosa before and after radiation exposure. After quality control to exclude low-quality cells, the dataset comprised approximately 28,189 cells. Graph-based clustering and cell marker annotation identified nine major cell types: epithelial cells, fibroblasts, endothelial cells, immune cells, Schwann cells, smooth muscle cells, pericytes, endo-pericytes, and myocytes (Fig. 1i and Supplementary Fig. 1d, e). Normalized transcriptomic analysis revealed differential expression of cell-defining genes across compartments, with gene expression patterns largely conserved across mucosal sites (Supplementary Fig. 1f). Radiation exposure led to a marked alteration in cell composition, notably a sharp reduction in epithelial cell numbers (Fig. 1j). To further characterize epithelial cell dynamics, these cells were categorized into four subpopulations: basal cells, spinous cells, granular cells, and corneocytes (Fig. 1k and Supplementary Fig. 1g). Basal epithelial cells, which are essential for maintaining mucosal homeostasis and mediating tissue repair, constituted the dominant epithelial subpopulation both before and after radiation exposure (Fig. 1l and Supplementary Fig. 1h, i). Understanding the dynamic changes in basal cells is therefore critical for elucidating the mechanisms of radiation-induced mucosal injury. KRT14, KRT5, and KRT15 are well-established markers of epidermal and oral basal cells[13]. Single cell
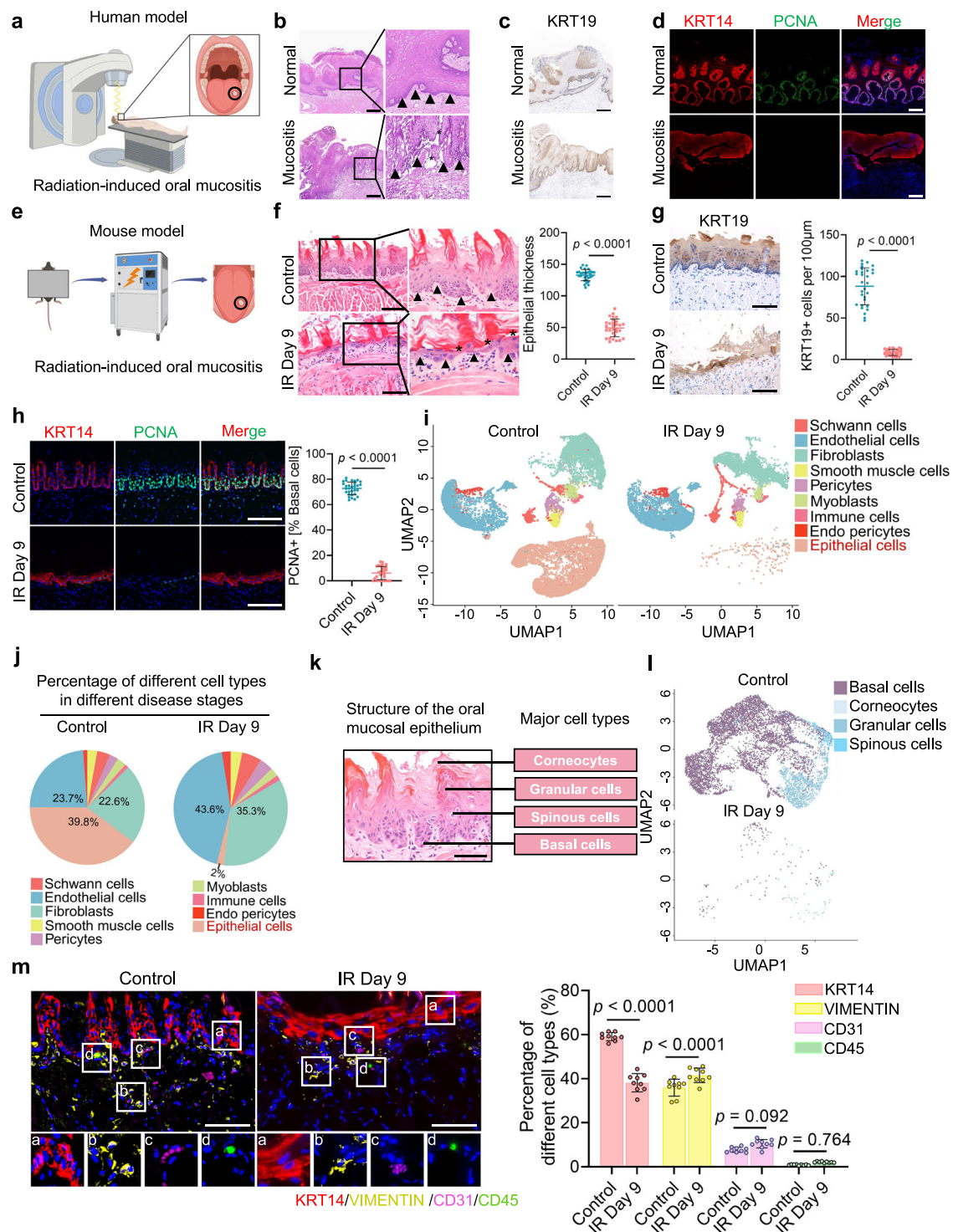
RNA sequencing and immunofluorescence co-localization analyses demonstrated spatial overlap between the expression of these markers and the basal cell layer (Supplementary Fig. 1j, k). Moreover, immunohistochemical staining for KRT14 confirmed a substantial reduction in basal cells post-radiation (Supplementary Fig. 1l). Finally, histological imaging revealed the presence of four major cellular compartments, epithelial basal cells, fibroblasts, endothelial cells, and immune cells, within the oral mucosal tissue, offering valuable insight into the local tissue architecture (Fig. 1m). Collectively, these findings demonstrate that ionizing radiation causes significant thinning of the oral mucosa, primarily due to severe depletion of epithelial cells, especially basal cells.

The impact of ionizing radiation on ferroptosis in basal epithelial cells

Different cell death pathways were assessed using the AddModuleScore function to investigate the cause of basal cell depletion. Notably, ferroptosis scores were significantly elevated following radiation exposure (Fig. 2a). Consistent with this finding, immunofluorescence analysis of acyl-CoA synthetase long-chain family member 4 (ACSL4), a key enzyme involved in polyunsaturated fatty acid activation and a known inducer of ferroptosis[14], revealed increased expression in basal cells from human oral mucositis lesions (Fig. 2b). To directly validate the role of ferroptosis, we administered the ferroptosis inhibitor LIP-1, which not only suppressed ACSL4 expression but also restored mucosal thickness (Fig. 2c-e). In vitro experiments further confirmed that radiation exposure led to reduced proliferation and increased mortality of basal cells (Supplementary Fig. 2a-c). We next evaluated the effects of several cell death inhibitors, including the ferroptosis inhibitor ferrostatin-1 (Fer-1), the apoptosis inhibitor Z-Val-Ala-Asp fluoromethylketone (Z-VAD-fmk), the necroptosis inhibitor necrostatin-1 (Nec-1s), and the pyroptosis inhibitor Belnacasan (VX-765), on the survival of irradiated basal cells. Treatment with Fer-1 or Z-VAD-fmk partially restored the clonogenic survival of basal cells following radiation exposure, with ferroptosis inhibitors demonstrating a more pronounced protective effect compared to the other inhibitors (Supplementary Fig. 2d). Mechanistically, radiation exposure significantly increased ROS levels and expanded the labile iron pool within basal cells, both of which were markedly reduced by Fer-1 treatment (Supplementary Fig. 2e, f). Furthermore, lipid peroxide accumulation, a hallmark of ferroptosis, was clearly detected and effectively suppressed by Fer-1 (Supplementary Fig. 2g). Collectively, these findings support ferroptosis in basal epithelial cells as a principal mechanism of radiation-induced cell death.

Potential early-stage protective compensation in RIOM

Murine tongue mucosal specimens were analyzed at sequential time points to elucidate the dynamic changes in basal cell ferroptosis following radiation exposure. Notably, the expression of prostaglandin-endoperoxide synthase 2 (PTGS2), a well-established biomarker of ferroptosis[15], did not significantly increase in basal cells during the early phase post-radiation, but was markedly elevated in the late phase (Fig. 2f). Importantly, this early phase was characterized by increased mucosal thickness and pronounced basal cell proliferation without significant DNA damage, suggesting a state of early hyperactivity in RIOM (Fig. 2g and Supplementary Fig. 3a-c). Additionally, scRNA-seq revealed an increase in basal cell numbers during the early phase, followed by a notable decline in the late phase (Supplementary Fig. 3d-f). In parallel, gene set variation analysis (GSVA) of basal cells indicated the activation of processes related to the response to toxic substances, enzymatic activity, and protein folding in the early post-radiation phase. There was also evidence of regulatory mechanisms that suppress apoptosis (Fig. 2h and Supplementary Fig. 3g). By contrast, in the late phase, GSVA revealed a decline in functions associated with protein folding, wound healing, cell-cell adhesion, translation, and

basement membrane integrity (Fig. 2h and Supplementary Fig. 3h). Collectively, these findings indicate the existence of a transient protective response during the early phase of RIOM, characterized by compensatory mucosal thickening aimed at counteracting radiation-induced stress. However, the specific molecular mechanisms underlying this protective effect remain to be fully elucidated.

Effect of fibroblasts on basal cell ferroptosis

Basal cells are regulated by localized cues within their microenvironment[16]. Understanding the cellular and molecular environment that governs post-injury repair is essential for maintaining basal cell homeostasis and promoting mucosal regeneration[17]. To investigate the protective mechanisms acting on basal cells during the early phase of RIOM, we analyzed the cellular components of the surrounding microenvironment. Notably, fibroblasts adjacent to basal cells not only declined significantly in number during the late phase (Fig. 3a, b) but also underwent a functional transition towards senescence, as suggested by Kyoto Encyclopedia of Genes and Genomes (KEGG) analysis (Supplementary Fig. 4a). Further evidence for this is provided by the elevated expression of the senescence markers $p16$ and $p21$ in murine glossal fibroblasts at 9 days post-radiation (Supplementary Fig. 4b). The dynamic changes in fibroblast populations align with the transition from compensatory to decompensatory phases, suggesting that fibroblasts may exert protective effects during

Fig. 1 | Radiation-induced epithelial thinning and basal cell depletion in human and murine glossal mucosa. a Glossal tissue specimens were collected from patients with head and neck malignant tumors undergoing surgery after radiotherapy. Created in BioRender. Yu, W. (2025) https://BioRender.com/xwdxw8b. **b** Changes in the glossal mucosa analyzed using hematoxylin and eosin (H&E) staining (*n* = 6 human samples). Epithelial depth was measured on H&E-stained sections by identifying the basal epithelial layer (cuboidal cells with hyperchromatic nuclei and tightly packed arrangement), and then quantifying the vertical distance from the basement membrane (a wavy boundary separating the epithelium from the stroma) to the epithelial surface. ▲ represents the boundary between the epithelium and stroma, * represents disruption of epithelial continuity. Scale bar, 500 μm. **c** Immunohistochemistry of human glossal tissue using Keratin 19 (KRT19) showed changes in epithelial thickness and morphology (*n* = 6 human samples). Scale bar, 500 μm. **d** Proliferating cell nuclear antigen (PCNA) immunofluorescence staining of human glossal tissue before and after exposure to ionizing radiation (*n* = 6 human samples). Scale bar, 500 μm. **e** Schematic diagram for the construction of a mouse animal model of radiation-induced oral mucositis. Created in BioRender. Yu, W. (2025) https://BioRender.com/j8wb6pl. **f** H&E staining of mouse tongues before and after irradiation. ▲ represents the boundary between

the epithelium and stroma, * represents disruption of epithelial continuity (*n* = 10 mice). Three random images per mouse were analyzed. Scale bar, 100 μm. **g** Sections from normal murine glossal mucosa and ulcerated areas near irradiated glossal tissues (*n* = 6 mice). Five random images per mouse were analyzed. Scale bar, 100 μm. **h** PCNA immunofluorescence staining of murine glossae before and after exposure to ionizing radiation (*n* = 6 mice). Five random images per mouse were analyzed. Scale bar, 100 μm. **i** Uniform manifold approximation and projection (UMAP) plots and annotations by major cell type from single-cell transcriptome analysis of murine glossal mucosa before and after irradiation. **j** Pie charts showing the percentages of different cell types before and after irradiation. **k** Diagram of the oral mucosal epithelium structure and major cell types. Scale bar, 50 μm. **l** UMAP plots and annotations by major epithelial cell type from single-cell transcriptome analysis of murine glossal mucosa before and after radiation. **m** Immunofluorescence depicted major cell types proportion in murine glossal mucosa before and after irradiation (*n* = 3 mice). Three random images per mouse were analyzed. Data represent the mean ± SD. Scale bar, 50 μm. Statistical significance was determined by unpaired two-tailed Student's *t* test (**f-h**). Statistical significance was determined by Two-way ANOVA analysis with Tukey's multiple comparisons test (**m**). Source data are provided as a Source Data file.

---

the compensatory stage. To further characterize fibroblast-basal cell interactions, we performed scRNA-seq coupled with CellChat analysis, which illustrated communication trends between cell types (line thickness indicates interaction strength). A sustained, high level of interaction was observed during the early phase, followed by a marked decline in the late phase (Fig. 3c). To validate the potential protective role of fibroblasts, we conducted in vitro co-culture experiments (Fig. 3d). Basal cells co-cultured with fibroblasts under irradiation conditions showed significantly enhanced proliferative activity compared to basal cells cultured alone (Fig. 3e). Furthermore, co-culture with fibroblasts led to reduced intracellular iron levels and decreased lipid peroxidation in irradiated basal cells (Fig. 3f-h). These findings indicate that fibroblast-mediated support plays a critical role in the early compensatory protection of basal cells against radiation-induced mucosal injury.

To elucidate the protective mechanisms of fibroblasts, we performed functional analyses, which revealed distinct clustering patterns at different post-radiation time points. Along the fibroblast differentiation trajectory, differential gene expression was observed (Fig. 3i and Supplementary Fig. 4c). In the early phase, genes associated with metabolism and epithelial protection (e.g., *ODC1*, *CRCT1*, *SLPI*) were upregulated, while inflammation-related genes (e.g., *CCL4*, *CXCL13*, *LCN2*) were enriched in the late phase (Supplementary Fig. 4d). These transcriptional dynamics were consistent with the functional transition observed: fibroblasts exhibited active metabolic roles in the early phase following radiation exposure, then shifted toward immune-related functions in the late phase (Fig. 3j). Together, these results suggest that fibroblasts provide early protective support to basal cells via metabolic regulation. However, the concomitant reduction in fibroblast numbers, in tandem with their senescence-associated functional transformation, diminishes this support, thereby exacerbating mucosal injury.
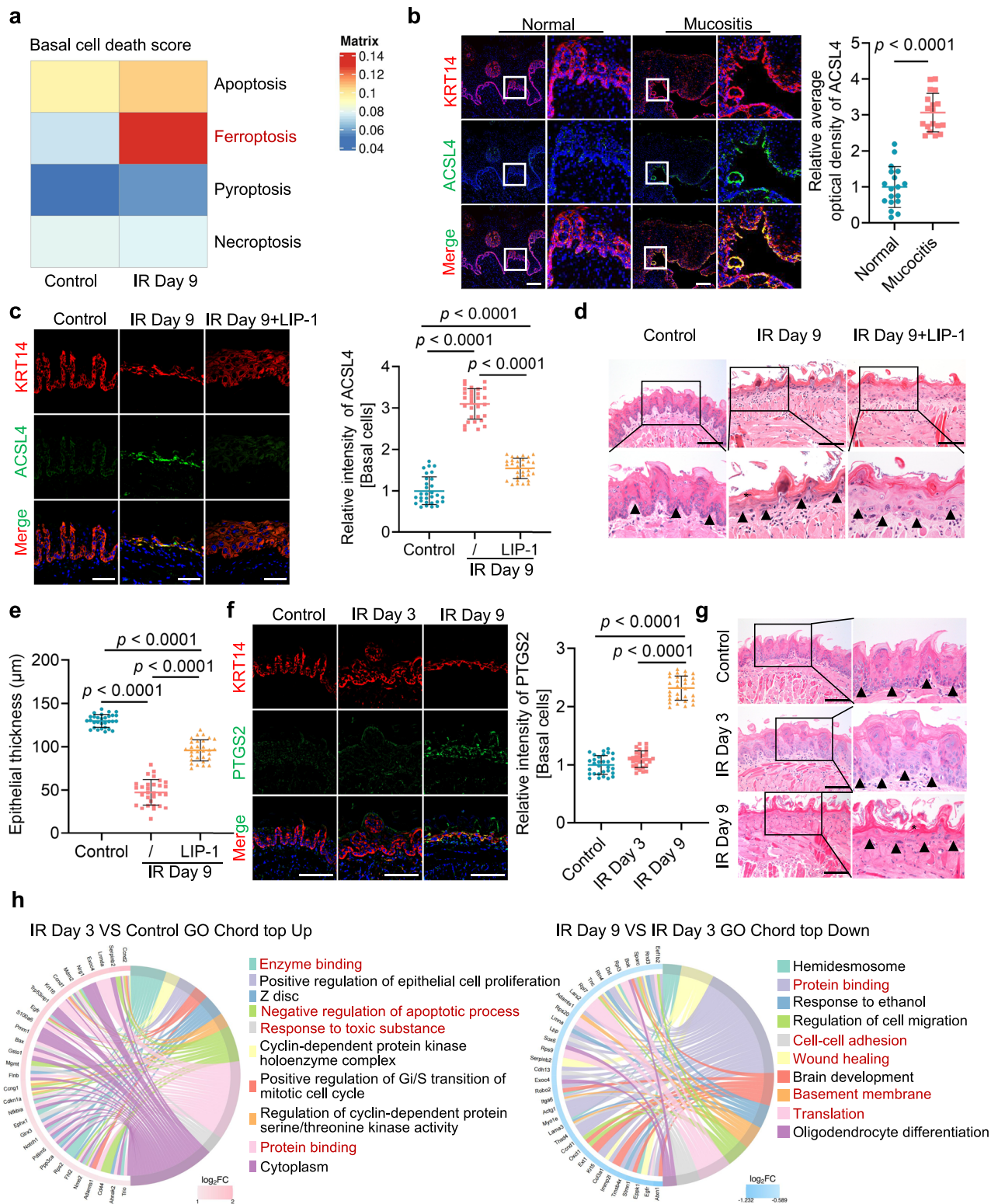
Mechanism of fibroblasts inhibit SAT1-ACSL4 ferroptosis pathway

The mechanism by which fibroblasts inhibit ferroptosis was subsequently investigated. On the ninth day post-irradiation, scRNA-seq analysis identified several ferroptosis-related differentially expressed genes in basal cells. Among these, *SAT1* (spermidine/spermine N1-acetyltransferase 1), *ACSL4*, and *SLC39A14* (solute carrier family 39 member 14) showed the most significant upregulation (Fig. 4a). Further validation using co-cultures of basal cells with fibroblasts revealed that fibroblasts exerted the strongest inhibitory effect on *SAT1* expression (Fig. 4b). Additionally, interference with *SAT1* led to a reduction in lipid peroxidation levels in basal cells (Supplementary

Fig. 5a). In vivo immunostaining of tongue tissues confirmed that SAT1 expression remained relatively unchanged during the early phase post-radiation but was markedly elevated in the late phase (Supplementary Fig. 5b). This temporal expression pattern suggests a potential association between the upregulation of SAT1 and the decline of fibroblast-mediated protection during the later stages of RIOM progression. Likewise, in the absence of fibroblast co-culture, irradiated basal cells exhibited a pronounced elevation of SAT1 protein levels (Supplementary Fig. 5c). Time-course co-culture experiments revealed a dynamic interaction: SAT1 expression significantly declined at 24 hours, indicating a rapid and transient protective effect of fibroblasts. However, this protective effect was no longer evident by 48 hours, and the decompensated state persisted through 72 hours (Fig. 4c and Supplementary Fig. 5d). Based on this, 24 hours was designated as the optimal time point for observing early protective effects, while 48 hours represented the onset of decompensation in the co-culture model. These findings suggest that fibroblasts inhibit ferroptosis in basal cells by suppressing SAT1 expression. To further explore the role of SAT1 in radiation-induced ferroptosis in vivo, *SAT1*-deficient mice were utilized. These mice exhibited preserved mucosal epithelial thickness and resistance to radiation-induced injury (Fig. 4d and Supplementary Fig. 5e). Additionally, their basal cells maintained high proliferative capacity in the late phase post-radiation (Fig. 4e). These results confirm that SAT1 contributes to radiation-induced injury and underscore the importance of fibroblast-mediated suppression of SAT1 during the early phase of exposure.

Next, we investigated the downstream targets of SAT1. Previous studies have shown that arachidonate 15-lipoxygenase (ALOX15) is a downstream effector of *SAT1* that promotes membrane lipid peroxidation and ferroptosis[18,19]. However, neither scRNA-seq nor immunofluorescence detected *ALOX15* expression in basal cells (Fig. 4f and Supplementary Fig. 5f), prompting a reassessment of the downstream pathways involved. Protein interaction analysis of ferroptosis-related differentially expressed genes in basal cells revealed ACSL4 as the most strongly interacting partner of SAT1 (Fig. 4g). This relationship was further evaluated by silencing *SAT1* and *ACSL4* using small interfering RNAs (siRNAs). Knockdown of SAT1 significantly suppressed ACSL4 expression, whereas silencing ACSL4 had negligible impact on SAT1 levels (Fig. 4h). In *SAT1*-deficient mice exposed to radiation, only a marginal increase in ACSL4 expression was observed during the late phase (Fig. 4i), reinforcing the idea that SAT1 exerts upstream regulatory control over ACSL4.

Finally, the effect of fibroblasts on ACSL4 expression was assessed. Co-culture with fibroblasts resulted in a marked decrease in ACSL4 levels in basal cells, but this suppressive effect

diminished over time. ACSL4 expression rebounded after its initial post-radiation decline, mirroring the time-dependent trend observed for SAT1 (Fig. 4j and Supplementary Fig. 5g). Together, these in vitro and in vivo findings demonstrate that fibroblasts mediate early compensatory protection in RIOM by alleviating ferroptosis in basal cells through suppression of the SAT1-ACSL4 axis. However, this protective mechanism diminishes during the late phase, thereby exacerbating ferroptosis and contributing to disease progression.

Fibroblasts sustain basal cells through dynamic paracrine polyamine transfer

Fibroblasts exhibit increased metabolic activity during the early phase following radiation exposure and are known to regulate SAT1, a key enzyme involved in polyamine metabolism[20,21] (Fig. 5a). This observation led to the hypothesis that fibroblasts may regulate SAT1 through the secretion of polyamines. To test this, polyamine metabolism in fibroblasts was assessed using the scMetabolism analytical tool.

Fig. 2 | Ionizing radiation induces ferroptosis in basal epithelial cells. a Heat map showing AddModuleScore for apoptosis, ferroptosis, pyroptosis, and necrosis in basal epithelial cells. **b** Representative images of ACSL4 expression in basal cells of normal human tissue and radiation-induced glossal mucositis tissue ($n = 6$ human samples). Three random images per human were analyzed. **c-e** C57BL/6 mice were treated with LIP1 (5 mg/kg) intraperitoneally, starting 7 days before irradiation and for 9 days post-irradiation. **c** Representative images of ACSL4 expression in basal cells of murine glossal tissues before and 9 days post-irradiation ($n = 6$ mice). Five random images per mouse were analyzed. Scale bar, 100 μm. **d, e** H&E staining images were taken to display changes in mucosal thickness and morphology ($n = 10$ mice). ▲ represents the boundary between the epithelium and stroma, * represents disruption of epithelial continuity. Three random images per mouse were analyzed. Scale bar, 100 μm. **f** Representative images of PTGS2

expression in basal cells of murine glossal tissues before and at 3- and 9-day post-irradiation ($n = 6$ mice). Five random images per mouse were analyzed. Scale bar, 100 μm. **g** Representative H&E staining of the morphology and thickness of murine epithelial mucosa before and at 3- and 9-day post-irradiation ($n = 10$ mice). ▲ represents the boundary between the epithelium and stroma, * represents disruption of epithelial continuity. Scale bar, 100 μm. **h** Chord diagram showing upregulated genes and gene ontology pathways in basal cells when comparing normal tissue with tissue 3 days post-radiation, and comparing tissue 3 days post-radiation with tissue 9 days post-radiation. Data represent the mean ± SD. Statistical significance was determined by unpaired two-tailed Student's t test (**b**). Statistical significance was determined by One-way ANOVA test with Tukey's multiple comparisons test (**c, e, f**). Source data are provided as a Source Data file.

Results revealed elevated polyamine metabolic activity in fibroblasts during the early post-radiation phase, which gradually declined over time (Supplementary Fig. 6a). These findings were further supported by immunofluorescence staining for spermidine/spermine in basal cells and liquid chromatography-mass spectrometry (LC-MS) analysis of tongue fibroblasts. Both techniques indicated that polyamine homeostasis was effectively maintained during the early phase following irradiation. In contrast, this compensatory mechanism eventually failed in both human and murine mucositis tissues during the late phase, leading to the observed decline in spermidine/spermine levels (Fig. 5b, c and Supplementary Fig. 6b, c). Moreover, LC-MS analysis of tongue fibroblasts from *SAT1*-knockout (KO) mice showed elevated polyamine concentrations following radiation, thereby supporting a negative regulatory role of SAT1 in polyamine metabolism (Supplementary Fig. 6d).

To further investigate polyamine dynamics between fibroblasts and basal cells, polyamine content was compared under different culture conditions following radiation. When cultured independently, radiation induced an increase in polyamine levels within fibroblasts, while polyamine levels decreased in both basal cells and their surrounding supernatant. However, basal cells co-cultured with fibroblasts exhibited an initial rise in spermidine/spermine levels, followed by a decline at later stages (Fig. 5d and Supplementary Fig. 6e, f). Notably, putrescine levels in basal cells remained elevated during the early phase after radiation exposure and declined in the later phase. Compared to monoculture, basal cells co-cultured with fibroblasts exhibited higher polyamine levels during the early phase (Supplementary Fig. 6g). These dynamics suggest that fibroblasts function as a metabolic support system by exporting newly synthesized polyamines to replenish the radiation-induced depletion in basal epithelial cells.
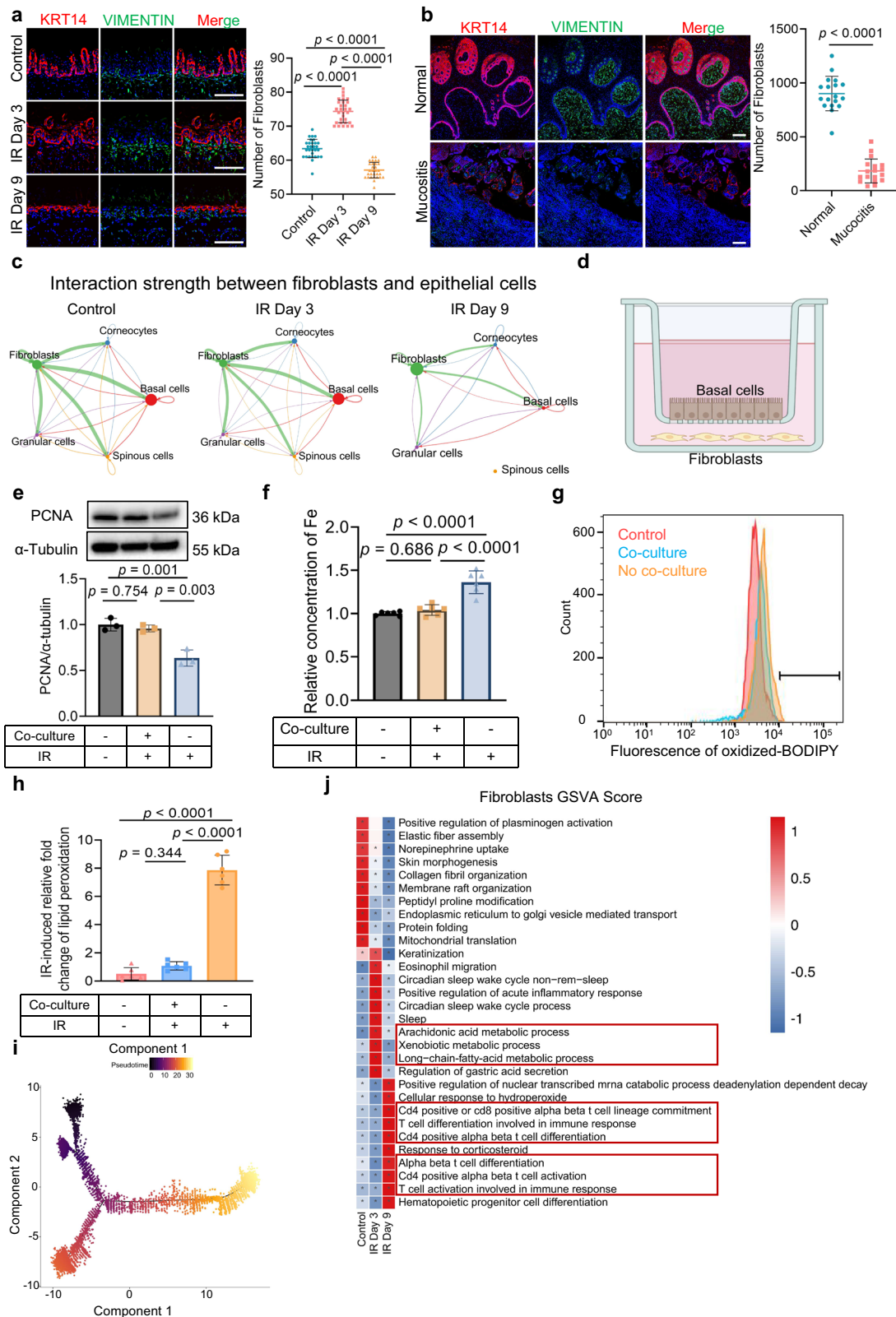
ODC1-mediated polyamine production in fibroblasts protects against radiation-induced ferroptosis in basal cells

Having established this supportive role of fibroblasts, we next investigated the regulatory mechanism behind polyamine synthesis. We found that ornithine decarboxylase 1 (ODC1), a key enzyme in the polyamine synthesis pathway[22,23], was substantially upregulated following radiation exposure (Fig. 5e). This upregulation was confirmed at the protein level via immunofluorescence, which showed a marked reduction in ODC1 expression in fibroblasts isolated from late-stage RIOM mice (Fig. 5f and Supplementary Fig. 7a), suggesting a potential exhaustion of this protective response over time. While ODC1 governs polyamine synthesis, we reasoned that the catabolic pathway must equally influence net polyamine levels. To test this and genetically validate the functional impact of altered polyamine metabolism, we turned to a model of disrupted catabolism by examining *SAT1* KO mice. In these mice, quantitative in vivo staining revealed a significant increase in fibroblast density as early as day 3 post-irradiation, an effect that persisted through day 9 (Supplementary Fig. 7b, c). Mechanistically, *SAT1* deficiency disrupted polyamine catabolism, leading to elevated tissue polyamine levels that directly promoted fibroblast

proliferation (Supplementary Fig. 7b, c). Phenotypically, the increased mucosal thickness observed in *SAT1* KO mice was associated with fibroblast expansion and polyamine accumulation. Therefore, while radiation-induced ODC1 expression in wild-type fibroblasts sustains polyamine homeostasis through de novo synthesis, *SAT1* deletion enhances polyamine retention by blocking catabolism. These complementary findings establish that the ODC1/SAT1 balance critically determines polyamine dynamics and mucosal outcomes after radiation.

To directly test the functional necessity of ODC1, we employed an in vivo knockdown approach in murine lingual fibroblasts using adeno-associated virus (AAV)-mediated gene delivery (Fig. 5g). Quantitative immunofluorescence confirmed selective ODC1 reduction in fibroblasts (Supplementary Fig. 8a). Histopathological analysis of ODC1 knockdown mice on post-radiation days 3 and 5 revealed accelerated mucosal thinning (Fig. 5h and Supplementary Fig. 8b), while PCNA immunostaining showed impaired basal cell proliferation (Supplementary Fig. 8c). In parallel, immunostaining and LC-MS analysis demonstrated reduced polyamine levels in basal cells and tongue fibroblasts, respectively (Fig. 5i and Supplementary Fig. 8d, e), directly linking ODC1 deficiency to disrupted polyamine biosynthesis. Mechanistically, these effects were accompanied by a significant increase in the expression of ferroptosis markers SAT1 and ACSL4 (Supplementary Fig. 8f-h), suggesting that fibroblast-derived ODC1-suppresses ferroptosis in basal cells by promoting polyamine production. These findings were further complemented by pharmacological inhibition with difluoromethylornithine (DFMO), which recapitulated the mucosal thinning and proliferation defects (Supplementary Fig. 9a–c). Furthermore, the DFMO model uncovered that polyamine depletion triggers premature ACSL4 activation, leading to its upregulation (Supplementary Fig. 9d).

To further corroborate these findings, *ODC1* knockdown was performed in fibroblasts in vitro (Supplementary Fig. 9e), followed by co-culture with basal cells prior to radiation exposure. The supernatant from ODC1-expressing fibroblasts contained higher levels of spermidine/spermine, whereas *ODC1* knockdown significantly reduced spermidine concentrations (Fig. 5j and Supplementary Fig. 9f). In addition, *ODC1*-deficient fibroblasts failed to suppress radiation-induced expression of SAT1 and ACSL4 in basal cells (Fig. 5k and Supplementary Fig. 9g). These results confirm that fibroblasts regulate polyamine levels in basal cells through a paracrine mechanism. We next sought to elucidate the mechanism underlying radiation-induced ODC1 activation. Previous studies have reported that HIF-1α acts as an upstream transcription factor of ODC1[24], and that radiation can induce hypoxia, thereby triggering HIF-1α activation[25]. Initial GO analysis further indicated a potential hypoxic response (Supplemental Fig. 9h), prompting us to hypothesize HIF-1α involvement. Radiation exposure was confirmed to activate HIF-1α (Supplemental Fig. 9i), and HIF-1α knockdown attenuated ODC1 induction (Supplemental Fig. 9j, k). Computational analysis of the ODC1 promoter using JASPAR database identified a conserved HIF-1α binding motif (Supplemental Fig. 9l, m).

Direct binding was subsequently validated through ChIP-qPCR, which demonstrated significant HIF-1α enrichment at the ODC1 promoter that was further enhanced following irradiation (Supplemental Fig. 9n). Collectively, these findings establish that radiation triggers HIF-1α-mediated transcriptional activation of ODC1, thereby completing the mechanistic pathway from radiation exposure to ODC1 upregulation.

To further evaluate the effects of polyamine supplementation on post-radiation basal cells, CCK-8 cell viability assays were performed. The results revealed a concentration-dependent biphasic effect on cell viability (Supplementary Fig. 10a). In vivo validation further demonstrated that high-dose spermidine aggravated mucosal injury, significantly suppressed basal cell proliferation (Supplementary Fig. 10b, c), and elevated the expression of ferroptosis markers SAT1 and ACSL4

Fig. 3 | Fibroblasts protect basal cells in the early stage of radiation-induced mucositis. a Representative images showing changes in the number of fibroblasts within the murine mucosa and their relationship with basal cells via immunofluorescence staining (*n* = 6 mice). Five random images per mouse were analyzed. Scale bar, 100 μm. **b** Representative images and analysis showing changes in the number of fibroblasts within normal human glossal tissue and radiation-induced glossal mucositis tissue via immunofluorescence staining (*n* = 6 human samples). Three random images per human were analyzed. Scale bar, 500 μm. **c** Circos plot showing the analysis of directed interaction intensity between fibroblasts and epithelial cell subgroups before and at 3- and 9-day post-irradiation. **d** Schematic of the in vitro co-culture system between fibroblasts (bottom) and basal cells (top). Created in BioRender. Yu, W. (2025) https://BioRender.com/68nkut8. **e** Western blot analysis of PCNA expression in basal cells 24 hours after exposure to 8 Gy radiation with or without prior co-culture with fibroblasts (*n* = 3 biologically independent experiments). **f** Total iron concentration in basal cells 24 hours after exposure to 8 Gy radiation, with or without prior co-culture with fibroblasts (*n* = 6 biologically independent samples). **g, h** Assessment of lipid peroxidation in basal cells 24 hours after exposure to 8 Gy radiation with or without prior co-culture with fibroblasts (*n* = 6 biologically independent samples). **i** Pseudotime trajectory plot of fibroblast differentiation in two-dimensional state space before and at 3- and 9-day post-irradiation. **j** Heat map showing Standardized Gene Set Enrichment analysis scores for selected gene ontology pathways in each fibroblast subtype. Data represent the mean ± SD. Statistical significance was determined by unpaired two-tailed Student's *t* test (**b**). Statistical significance was determined by One-way ANOVA test with Tukey's multiple comparisons test (**a**, **e**, **f**, and **h**). Source data are provided as a Source Data file.

(Supplementary Fig. 10d, e). Conversely, in vitro experiments showed that physiological (low) concentrations of polyamines inhibited *SAT1* expression by reducing lipid peroxidation, thereby suppressing ferroptosis. In contrast, cytotoxic high concentrations promoted ferroptosis by enhancing lipid peroxidation (Supplementary Fig. 10f, g). Supporting these observations, pretreatment of basal cells with low concentrations of spermidine or spermine prior to radiation exposure significantly suppressed the expression of SAT1 and ACSL4 (Fig. 5l and Supplementary Fig. 10j), and reduced lipid peroxidation (Supplementary Fig. 10h, i). Collectively, these findings confirm that ODC1-dependent production of polyamines in fibroblast protect basal epithelial cells against radiation-induced ferroptosis by regulating the SAT1-ACSL4 axis in a dose-dependent manner.

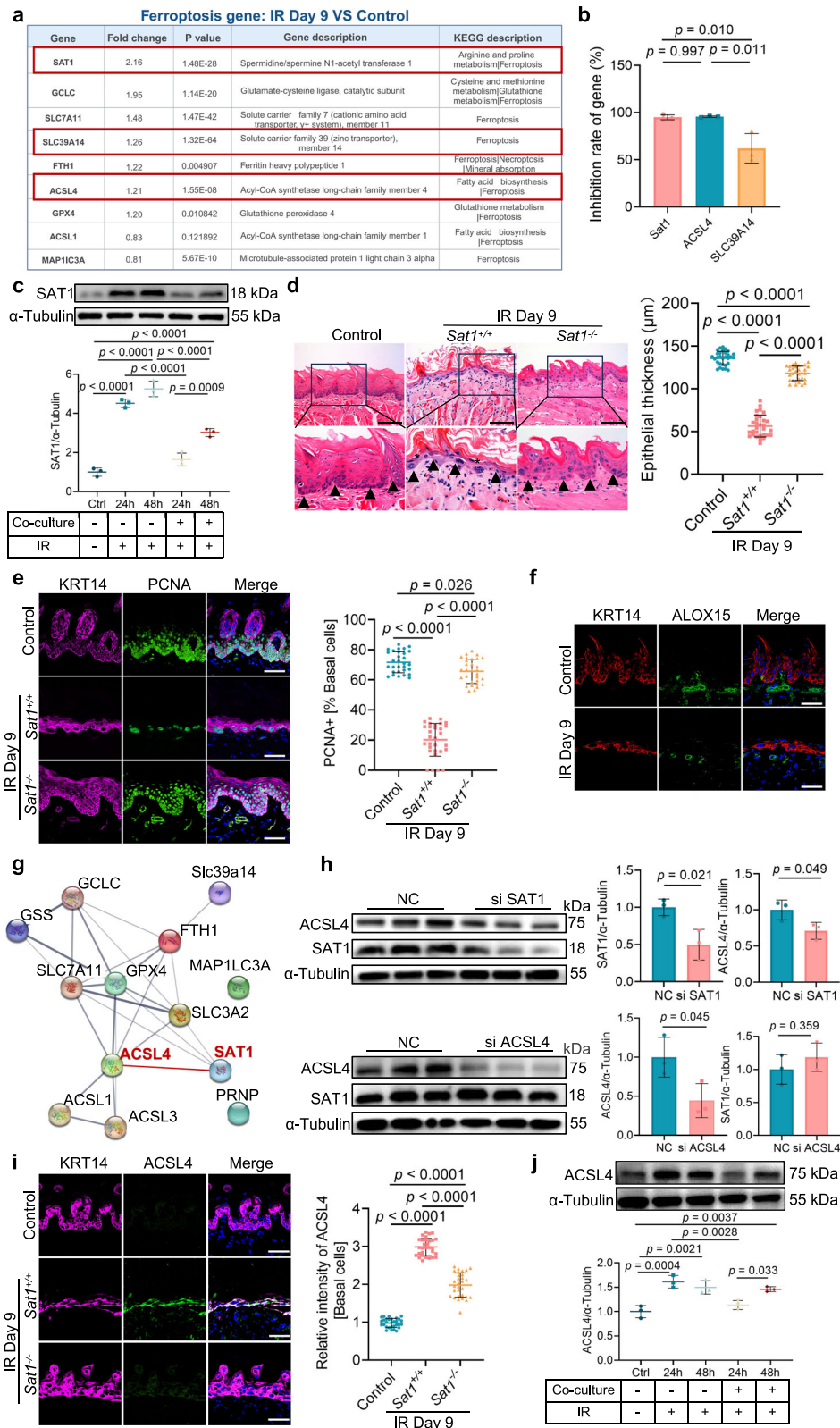## Polyamines in mucosal protection against ionizing radiation-induced damage

Given the ability of spermidine and spermine to inhibit basal cell ferroptosis during the early phase of RIOM, their potential as a preventive strategy against mucositis was investigated. Intraperitoneal injections of polyamines were administered starting before radiation exposure and continued through day 9 post-radiation. Tongue tissues were collected and analyzed on days 3 and 9 (Fig. 6a). Polyamine supplementation effectively suppressed JunD activation in basal cells through the late radiation phase (Fig. 6b), which corresponded with reduced *ACSL4* expression and markedly attenuated ferroptosis (Fig. 6c). To assess the therapeutic efficacy of polyamines in comparison to commonly used clinical treatments, two additional groups received either KGF-1 intraperitoneally or 0.15% benzydamine (BDM) mouthwash daily from 7 days before to 9 days after radiation exposure. Among all treatments, spermidine demonstrated the strongest therapeutic effect, surpassing that of the ferroptosis inhibitor LIP-1, spermine, KGF-1, and BDM. Immunofluorescence staining confirmed significantly enhanced epithelial proliferation in the spermidine-treated group by day 9 post-radiation (Fig. 6d and Supplementary Fig. 11a). Additionally, spermidine treatment resulted in greater mucosal thickness, improved basal layer architecture, and enhanced epithelial continuity in the late radiation phase (Fig. 6e). Long-term safety and efficacy were further validated. Follow-up to day 28 demonstrated sustained mucosal integrity without signs of recurrence (Supplementary Fig. 11b). Histological evaluations of heart, liver, and kidney tissues revealed no systemic toxicity (Supplementary Fig. 11c). Collectively, these findings demonstrate that spermidine supplementation effectively suppresses ferroptosis, promotes basal cell proliferation, and preserves mucosal integrity. This strategy holds promise as a therapeutic approach for preventing and managing RIOM.

We further explored the therapeutic potential of polyamines in mitigating damage to non-oral tissues during abdominal radiation. Mice were intraperitoneally injected with saline, spermidine (10 mg/kg), or amifostine (10 mg/kg), followed by a single 10 Gy dose of abdominal radiation. On day 8 post-radiation, colonic tissue was examined. Notably, the colons of spermidine-treated mice were significantly longer (Supplementary Fig. 12a), suggesting reduced inflammatory damage. These findings confirmed the protective effect of spermidine against radiation-induced colon injury. Histological analysis revealed that spermidine preserved colonic mucosal integrity and strengthened the integrity of the gut barrier, as evidenced by reduced penetration of FITC-dextran after oral administration (Supplementary Fig. 12b, c). Additionally, crypt base columnar stem cells exhibited enhanced proliferative capacity following spermidine treatment (Supplementary Fig. 12d). To further evaluate the role of spermidine in inhibiting ferroptosis, we assessed the expression of key ferroptosis-associated proteins in irradiated colonic tissues. A significant decrease in *ACSL4* expression was observed in the spermidine-treated group (Supplementary Fig. 12e, f), indicating that polyamines mitigate colon injury at least in part by suppressing ferroptosis. Beyond the colon, protective effects of spermidine were also observed in the liver and lungs. In the liver, spermidine treatment reduced vacuolar degeneration, while in the lungs, it lessened alveolar collapse following radiation exposure (Supplementary Fig. 12g). These findings demonstrate that spermidine exerts a broad protective effect against radiation-induced tissue injury.

Polyamines inhibit basal cell SAT1-ACSL4 ferroptosis pathway by inhibiting JunD-mediated transcriptional regulation

To further investigate the mechanism underlying the protective effects of polyamines, and given that polyamines are known to regulate gene expression via modulation of transcription factors[23,26,27], we hypothesized that they might influence the upstream transcription factors of SAT1. We analyzed scRNA-seq data using the Single-Cell Regulatory Network Inference and Clustering (SCENIC) platform to explore this, which identified JunD and JunB as candidate transcription factors regulating *SAT1*. Structurally, JunD and JunB exhibit significant homology (Fig. 6f and Supplementary Fig. 13a). Functional validation showed that disruption of either factor destabilized the protein complex. Notably, knockdown of JunD led to degradation of JunB protein (Supplementary Fig. 13b, c), indicating functional interdependence between these homologous factors[28]. Despite this, consistent with its stronger suppression of SAT1 expression upon depletion, compared to JunB knockdown (Supplementary Fig. 13b, c), JunD exhibited higher regulon activity than JunB (Supplementary Fig. 13d). Given that JunD expression was upregulated in murine basal cells during the late stage of radiation exposure (Supplementary Fig. 13e), we further examined its role in ferroptosis using siRNA-mediated knockdown. *JunD* knockdown significantly reduced lipid peroxidation levels in irradiated basal cells (Supplementary Fig. 13f). Notably, DFMO-treated basal cells exhibited premature JunD activation post-radiation (Supplementary Fig. 13g). Mechanistically, transcription factor binding analysis of the *SAT1* promoter using the JASPAR database identified JunD-binding sequences within the promoter region (Fig. 6g). Subsequent ChIP-qPCR confirmed increased enrichment of JunD at these sites, which was further enhanced by radiation exposure (Fig. 6h). Importantly, disruption of JunD led to substantial downregulation of both SAT1 and

ACSL4 protein levels (Fig. 6i and Supplementary Fig. 13h), confirming its upstream regulatory role. Together, these findings establish that JunD directly modulates SAT1 expression and that its activation plays a critical role in initiating ferroptosis in basal cells.

We next sought to determine how polyamines influence JunD expression. Our results revealed that polyamine supplementation markedly suppressed JunD expression, whereas DFMO-induced polyamine depletion led to an increase in JunD levels (Supplementary Fig. 13i). To further investigate the mechanism, we assessed JunD mRNA stability using actinomycin D to block transcription. We found that polyamine depletion significantly enhanced JunD mRNA stability, whereas spermidine supplementation markedly reduced it (Supplementary Fig. 13j). Together, these results indicate that polyamines regulate JunD expression through post-transcriptional control.

Fig. 4 | Fibroblasts inhibit ferroptosis in basal cells through suppression of the SAT1-ACSL4 pathway. a Table showing changes in ferroptosis-related gene expression in basal cells before irradiation and for 9 days post-irradiation. **b** qRT-PCR analysis of SAT1, ACSL4, and SLC39A14 inhibition rate in basal cells with or without prior fibroblast co-culture for 24 hours after exposure to 8 Gy irradiation (*n* = 3 biologically independent experiments). **c** Western blot analysis of SAT1 expression in basal cells cultured with or without fibroblasts for 24 hours and 48 hours after exposure to 8 Gy irradiation. (*n* = 3 biologically independent experiments). **d** Representative H&E staining of the oral mucosal epithelium of *Sat1*⁺/⁺ and *Sat1*⁻/⁻ mice before irradiation and for 9 days post-irradiation (*n* = 6 mice). Five random images per mouse were analyzed. ▲ represents the boundary between the epithelium and stroma, * represents disruption of epithelial continuity. Scale bar, 100 μm. **e** Immunofluorescence staining for PCNA expression in basal cells of *Sat1*⁺/⁺ and *Sat1*⁻/⁻ murine tongues before irradiation and for 9 days post-irradiation (*n* = 6 mice). Five random images per mouse were analyzed. Representative images are shown. Scale bar, 50 μm. **f** Immunofluorescence showing the location and expression of ALOX15 in wild-type mice before irradiation and for 9 days post-irradiation. Scale bar, 50 μm. **g** STRING protein-protein interaction network analysis of interactions among ferroptosis-related genes in basal cells. **h** Western blot analysis of SAT1 and ACSL4 expression in basal cells after irradiation, with or without siRNA-mediated knockdown of SAT1 or ACSL4 (*n* = 3 biologically independent samples). **i** Immunofluorescence staining for ACSL4 expression in basal cells of *Sat1*⁺/⁺ and *Sat1*⁻/⁻ mice before irradiation and for 9 days post-irradiation (*n* = 6 mice). Five random images per mouse were analyzed. Representative images are shown. Scale bar, 50 μm. **j** Western blot analysis of ACSL4 expression in basal cells prior cultured with or without fibroblasts for 24 hours and 48 hours after exposure to 8 Gy irradiation (*n* = 3 biologically independent experiments). Data represent the mean ± SD. Statistical significance was determined by unpaired two-tailed Student's *t* test (**h**). Statistical significance was determined by One-way ANOVA test with Tukey's multiple comparisons test (**b**-**e**, **i** and **j**). Source data are provided as a Source Data file.

Taken together, this study uncovers a sophisticated regulatory network involving fibroblast-secreted polyamines, JunD-mediated transcriptional control, and downstream modulation of the SAT1-ACSL4 ferroptosis pathway. In summary, polyamines suppress ferroptosis and confer protection against radiation-induced damage not only in the oral mucosa, but also in the colon, liver, and lungs. These results suggest that ferroptosis-targeted therapy using polyamines holds considerable promise for reducing normal tissue toxicity associated with radiotherapy (Fig. 6j).

Discussion

The prevention and treatment of RIOM must address the critical issue of epithelial ablation caused by extensive basal cell death[29]. Previous studies have shown that intense ionizing radiation induces DNA double-strand breaks, leading to cell cycle arrest, senescence, and multiple modes of cell death, including apoptosis, necrosis, autophagy, and mitotic catastrophe. Ferroptosis, a distinct form of iron-dependent cell death, is driven by the accumulation of lipid peroxides resulting from an imbalance in the cellular antioxidant system[30,31]. The present study demonstrates that radiation activates the SAT1-ACSL4 signaling axis. Consistent with earlier reports, SAT1 may function as a histone H3K27 acetyltransferase[32], directly enhancing chromatin accessibility at the ACSL4 locus through H3K27ac modification and thereby promoting ACSL4 transcription[33]. These findings provide a mechanistic explanation for the epithelial damage observed following extensive basal cell death induced by ionizing radiation. Radiation exposure triggers widespread ROS generation, and ferroptosis may propagate through ROS waves, transmitting oxidative stress over long distances within human cell populations[34,35]. The rupture of cell membranes during ferroptosis compromises the epithelial barrier, facilitating microbial invasion and infiltration of harmful substances. This, in turn, activates monocyte-mediated inflammatory responses and the release of pro-inflammatory cytokines, further exacerbating tissue injury[36,37].

This study found that low concentrations of polyamines in the physiological microenvironment inhibit SAT1 transcription by binding to the transcription factor JunD. This disrupts the SAT1-ACSL4 signaling axis, suppressing ferroptosis and enabling normal tissue repair. Notably, JunD activation is also driven by oxidative stress signals[38]. By inhibiting lipid peroxidation[39], the ferroptosis inhibitor LIP-1 reduces oxidative stress, thereby diminishing JunD activation and protein expression. These findings suggest that the regulation of JunD and ferroptosis is not unidirectional but governed by a dynamic redox-dependent feedback loop.

Interestingly, polyamines exhibit cell type- and concentration-dependent biphasic effects on ferroptosis. In cancer cells, elevated polyamine metabolism exacerbates lipid peroxidation via H_2O_2-dependen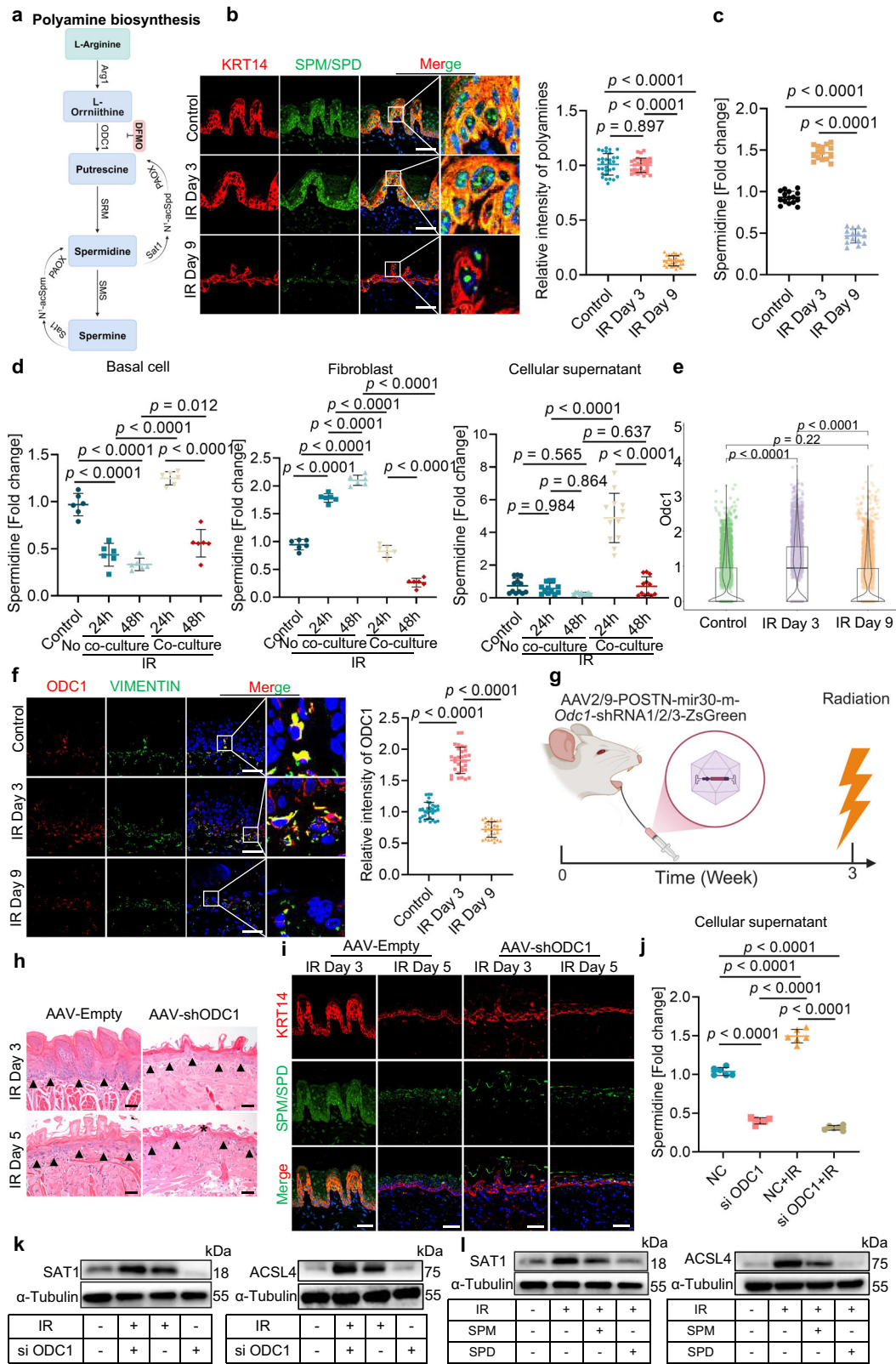t mechanisms, amplifying ferroptosis[40-42]. In contrast, in normal cells under oxidative stress, low concentrations of exogenous polyamines counteract ferroptosis and support cell proliferation[43,44]. This duality underscores the critical importance of maintaining polyamine homeostasis for precise biological outcomes. Consistently, the maintenance of such homeostasis—as evidenced by the stable polyamine levels observed at the early stage after irradiation—confers a pivotal protective effect. The absence of a significant decline further underlines their constitutive role in supporting epithelial survival under stress. Thus, polyamines serve not only as metabolic substrates for SAT1, but also as signaling molecules that dynamically regulate systemic homeostasis. Their concentration-dependent, bidirectional roles offer a theoretical basis for developing precision-targeted interventions in polyamine metabolism[45-47]. This study reveals a direct mechanistic link between polyamine metabolism and ferroptosis and proposes that polyamine-based strategies may represent a promising approach for protecting normal tissues from radiation-induced injury. These insights have broader implications beyond RIOM, extending to the prevention and treatment of radiation-induced damage in the skin, intestines, and other organs.

Despite the promising findings, this study has several limitations. Our use of a simplified in vitro co-culture system, while instrumental in establishing direct cell-cell communication, may not fully capture the complexity of the irradiated tissue microenvironment. The precise mechanism by which polyamines are transported from fibroblasts to basal epithelial cells remains unclear. Whether this transfer occurs via passive diffusion, extracellular vesicles[40], or ATP13A2-mediated lysosomal uptake[48] requires further experimental validation in irradiated tissues. Additionally, the functional dynamics of the polyamine signaling network are complex. Polyamines may influence post-radiation JUN signaling directly, potentially by promoting JUNB phosphorylation[49]. Moreover, existing literature indicates that polyamines facilitate the hypusination of eukaryotic translation initiation factor 5 A (eIF5A), a modification essential for cellular proliferation[50]. Given that spermidine serves as the direct substrate for this process, the hypusination pathway may represent an additional mechanism through which polyamines support stress responses and regeneration following radiation exposure. Future studies will aim to elucidate these mechanistic pathways. Addressing these knowledge gaps will be essential for optimizing polyamine-based therapeutic strategies to protect against radiation-induced tissue injury.

Methods
Mice

Sat1⁻/⁻ mice (C57BL/6N-Sat1em1cyagen, stock number: KOCMP-20229-Sat1-B6N) were generously provided from Prof Wei Zhao (Department of Medical Immunology, School of Basic Medical Sciences, Shandong University). Male C57BL/6 mice (6-8 weeks old) were obtained from the Laboratory Animal Research Center of the Fourth Military Medical

University. All animal studies were approved by the Institutional Animal Care and Use Committee at the Fourth Military Medical University (Ethical Approval Number: IACUC-2023-kq-066) and conducted in accordance with the NIH Guide for the Care and Use of Laboratory Animals. Anesthesia was performed using isoflurane, and euthanasia was carried out via CO_2 asphyxiation followed by cervical dislocation.

Human participants

Paraffin-embedded human tissue sections were obtained from the Third Affiliated Hospital of the Fourth Military Medical University. The specimens were collected from the lingual mucosa adjacent to irradiated areas in patients with oral cancer ($n = 6$). Unirradiated oral mucosal sections were obtained via tissue biopsy from tongue cancer patients, at least 5 cm away from the tumor margin ($n = 6$). All samples

Fig. 5 | Fibroblasts produce polyamines that inhibit ferroptosis in basal cells during the early phase of post-irradiation recovery. a Schematic of the polyamine metabolic pathway. **b** Representative immunofluorescence images showing spermidine and spermine content in basal cells of murine glossal tissues before and at 3- and 9-day post-irradiation ($n = 6$ mice). Five random images per mouse were analyzed. Scale bar, 100 µm. **c** Levels of spermidine produced by murine glossal fibroblasts before and at 3- and 9-day post-irradiation, measured by liquid chromatograph-mass spectrometer (LC-MS) ($n = 15$ biologically independent samples). **d** Levels of spermidine produced by basal cells, fibroblasts, and cellular supernatant before and after irradiation, measured by LC-MS when prior cultured with or without fibroblasts ($n = 6$ biologically independent samples). **e** Violin plot of ODC1 mRNA levels in fibroblasts before and at 3- and 9-day post-irradiation. **f** Quantification of ODC1 expression levels in fibroblasts of mice before and at 3- and 9-day post-irradiation ($n = 6$ mice). Five random images per mouse were analyzed. Scale bar, 100 µm. **g** Schematic illustration of adeno-associated virus (AAV)-mediated ODC1 knockdown in fibroblasts. Created in BioRender. Yu, W. (2025) https://BioRender.com/41794et. **h** H&E staining and quantitative analysis of epithelial thickness in murine mucosa from AAV-Empty and AAV-shODC1 groups at 3- and

5-days post-irradiation ($n = 5$ mice). ▲ represents the boundary between the epithelium and stroma, * represents disruption of epithelial continuity. Three random images per mouse were analyzed. Scale bar, 50 µm. **i** Representative immunofluorescence images showing spermidine/spermine content in basal cell from AAV-Empty and AAV-shODC1 groups at 3- and 5-days post-irradiation ($n = 5$ mice). Scale bar, 50 µm. **j** Levels of spermidine produced by cells and present in cellular supernatant, measured by LC-MS when cultured without irradiation, or 24 hours after exposure to 8 Gy irradiation, with or without prior ODC1 siRNA transfection ($n = 6$ biologically independent samples). **k** Western blot analysis of SAT1/ACSL4 expression in basal cells without radiation, or 24 hours after exposure to 8 Gy irradiation, with or without prior supplementation of spermidine and spermine ($n = 3$ biologically independent experiments). **l** Western blot analysis of SAT1/ACSL4 expression in basal cells without irradiation, or 24 hours after exposure to 8 Gy irradiation, with or without prior ODC1 siRNA transfection ($n = 3$ biologically independent experiments). Data represent the mean ± standard deviation. Statistical significance was determined by One-way ANOVA test with Tukey's multiple comparisons test. Source data are provided as a Source Data file.

were acquired with written informed consent, ensuring participants' full understanding of the research objectives and procedures. This study was formally approved by the Ethics Committee of the Third Affiliated Hospital of the Fourth Military Medical University (Ethical Approval Number: KQYJ2024160) and conducted in strict compliance with international ethical standards, including the principles of the Declaration of Helsinki.

Cell culture
Human oral epithelial cells (CM-H203) and oral fibroblasts (CM-H205) were obtained from Procell Life Science & Technology Co., Ltd. (Wuhan, China, https://www.procell.com.cn/). Human oral keratinocytes (HOK, PRI-H-00140) were acquired from Shanghai Zhongqiaoxinzhou Biotech (Shanghai, China, https://www.zqxzbio.com/). All cell types were isolated from oral mucosa using combined trypsin-collagenase IV digestion and purified by differential adhesion. Each vial contained 5×10^5 cells with >90% purity, confirmed by immunofluorescence staining (cytokeratin-18 for epithelial cells; vimentin for fibroblasts; cytokeratin-14 for keratinocytes). Cells were cultured in DMEM medium (Pricella, PM150210) supplemented with 10% fetal bovine serum (FBS, Pricella, 164210-50) and 1% penicillin-streptomycin (Pricella, PB180120) at 37 °C under a humidified atmosphere of 5% CO_2/95% air. Medium was replaced every 48-72 hours. Cells were passaged at 80-90% confluency using 0.25% Trypsin-EDTA (Gibco, 25200056). After trypsinization, cells were centrifuged at $1,000 \times g$ for 5 minutes at 4 °C, and the pellet was resuspended in fresh culture medium for subculture at a ratio of 1:3 to 1:4. All cells tested negative for HIV-1, HBV, HCV, mycoplasma, bacteria, yeast, and fungi.

Sample preparation for scRNA-seq
Tongue samples were collected from mice at 3 and 9 days post-irradiation, along with untreated control mice (10 mice per group). Samples were pooled by combining tissues from all mice in each experimental group. Under sterile conditions, tongues were washed twice in pre-chilled RPMI 1640 medium (Gibco, 11875119) supplemented with 0.04% bovine serum albumin (BSA, MACS, 1000076). After removing underlying muscle tissues on ice, the remaining tissues were finely minced into approximately 0.5 mm³ fragments using surgical scissors. Tissue fragments were transferred to a digestion mixture containing collagenase II (Gibco, 17018029) and hyaluronidase (0.5 mg/mL, Sigma-Aldrich, H1115000), then incubated at 37 °C in a water bath for 30-60 minutes with gentle inversion every 5-10 minutes to facilitate uniform enzymatic digestion. Post-digestion, cell suspensions were sequentially filtered through a 0.4 mm cell strainer (BD Biosciences) to remove undigested debris, followed by centrifugation at $300 \times g$ for 5 minutes at 4 °C. The cell pellet was resuspended in

culture medium, to which an equal volume of red blood cell lysis buffer (MACS, 130-094-183) was added. The mixture was gently mixed and left to stand at 4°C for 10 minutes to lyse any residual erythrocytes. Afterward, the suspension was centrifuged again at $300 \times g$ for 5 minutes, and the supernatant was discarded. The cell pellet was washed once with culture medium, followed by another centrifugation at $300 \times g$ for 5 minutes. The supernatant was removed, and the cell pellet was reconstituted in 100 µl of culture medium. Cell concentration and viability were determined using a Luna cell counter (Logos Biosystems). All raw sequencing data are publicly accessible via the NCBI database (SRR32273201; SRR32273200; SRR32305640).
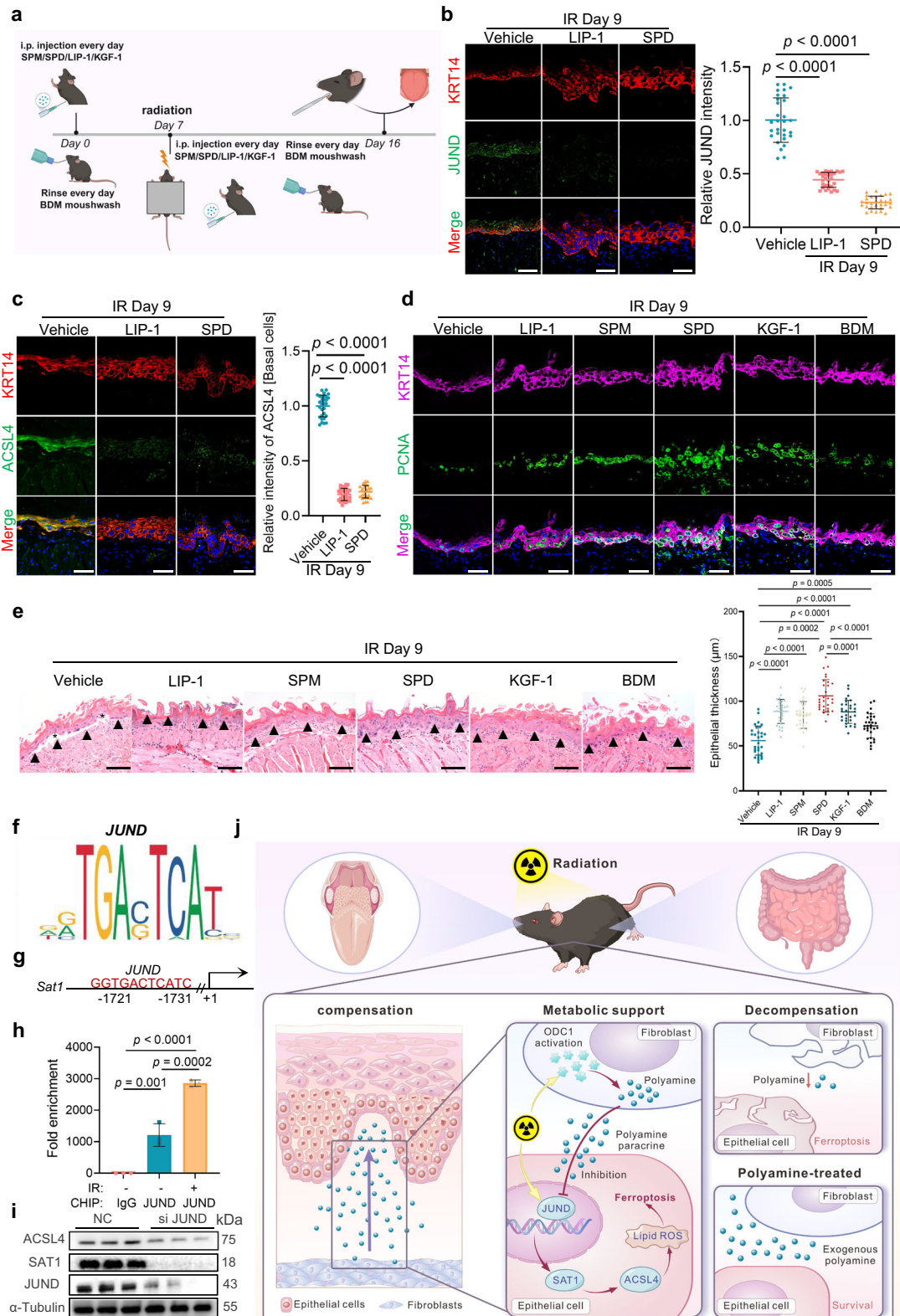
scRNA sequencing
Single-cell isolation and sequencing were performed at OE Biotech Co. Ltd. (Shanghai, China). Freshly prepared single-cell suspensions were adjusted to a concentration of 700 to 1200 cells per microliter according to the manufacturer's protocol. Library construction and instrument loading were carried out following the instructions provided with the Chromium Next GEM Single Cell 3' Reagent Kits v3.1 (10x Genomics). The resulting libraries were sequenced on an Illumina NovaSeq 6000 platform using paired-end 150 bp reads for high-throughput sequencing.

scRNA-seq data preprocessing and quality control
The scRNA-seq data was processed using the Cell Ranger software pipeline (version 7.0.1) provided by 10x Genomics for demultiplexing of cellular barcodes. Reads were aligned to the genome and transcriptome, and subsampling was performed as necessary to generate normalized aggregated data across samples, resulting in a gene count versus cell contrast matrix. We utilized the R package Seurat[51] (version 4.0.0) to handle the unique molecular identifier (UMI) count matrix. Quality control measures were applied to filter the cells based on the following criteria: a minimum number of detected genes greater than 200, a total UMI count exceeding 1000, a log10(GenePerUMI) value above 0.7, a mitochondrial UMI ratio below 10%, and a hemoglobin gene expression level less than 5%. After applying these quality control standards, a total of 41,810 cells met the criteria and were retained for downstream analysis.

Dimensionality reduction and cluster analysis
The identification of highly variable genes was performed using the FindVariableFeatures function from the Seurat package (version 4.0.0). The expression profiles of these selected HVGs were then leveraged to apply mutual nearest neighbor (MNN) correction, a technique aimed at mitigating batch effects present within the single-cell expression data. Following batch effect correction, the

multidimensional dataset was subjected to dimensionality reduction using uniform manifold approximation and projection (UMAP), a powerful non-linear technique, to visualize the corrected data in a two-dimensional space, facilitating the interpretation and exploration of cellular heterogeneity and structure. Marker genes for each cluster were identified using the FindAllMarkers function with test.use = 'presto'. Differential gene expression analysis was conducted using the FindMarkers function, also with

test.use = 'presto', setting a significance threshold of $P < 0.05$ and an absolute log2 fold change greater than 1.5 for differentially expressed genes. Enrichment analysis for these significantly differentially expressed genes was performed using hypergeometric tests for GO and Kyoto Encyclopedia of KEGG pathways. To quantify the activity of cell death gene signatures in epithelial and basal cells, the function "AddModuleScore" within Seurat was utilized.

Fig. 6 | Polyamines inhibit ferroptosis and reverse mucosal damage in basal cells. a Schematic diagram of treatment timing: Vehicle, LIP-1 (5 mg/kg), KGF-1 (6.25 mg/kg), spermidine (10 mg/kg), spermine (10 mg/kg) (all administered via intraperitoneal injection), and 0.15% benzydamine mouthwash (topical application), starting 7 days prior to irradiation and continuing until 9 days post-irradiation. Created in BioRender. Yu, W. (2025) https://BioRender.com/so7cr39. **b** Immunofluorescence showing the expression of JunD in basal cells before irradiation and for 9 days post-irradiation. Five random images per mouse were analyzed. Scale bar, 100 μm (*n* = 6 mice). **c** Immunofluorescence showing the expression of ACSL4 in basal cells before irradiation and for 9 days post-irradiation (*n* = 6 mice). Scale bar, 100 μm. **d** Quantification of PCNA+ basal cells before irradiation and for 9 days post-irradiation (*n* = 6 mice). Five random images per mouse were analyzed. Scale bar, 100 μm. **e** H&E staining and epithelial thickness of mouse mucosa before irradiation and for 9 days post-irradiation (*n* = 10 mice). ▲ represents the boundary between the epithelium and stroma, * represents disruption of epithelial continuity. Three random images per mouse were analyzed. Scale bar, 100 μm. **f** Consensus sequence for the JunD binding motif. **g** Presumed binding site of JunD in the promoter region of the SAT1 gene. **h** Fold enrichment of JunD binding in SAT1 gene promoter upon radiation treatment normalized to IgG control (*n* = 3 biologically independent experiments). **i** Western blot analysis of JunD, SAT1, and ACSL4 expression in basal cells after irradiation, with or without interference of the JunD gene (*n* = 3 biologically independent experiments). **j** Graphic abstract of the study. Created in Affinity Designer 2. Data represent the mean ± standard deviation. Statistical significance was determined by One-way ANOVA test with Tukey's multiple comparisons test. Source data are provided as a Source Data file.

GSVA
Firstly, background gene set files were retrieved and organized from the KEGG database (https://www.kegg.jp/) utilizing the GSEABase package (version 1.44.0). To assign pathway activity estimates to individual cells, we applied GSVA[52] using standard settings, as implemented in the GSVA package (version 1.30.0). Lastly, differential pathway activity between distinct groupings was quantified using the Linear Models for Microarray Data software package (version 3.38.3).

CellChat analysis
The cell communication analysis was performed using the CellChat[53] (version 1.1.3) R package. First, we imported the normalized scRNA-seq expression matrix to create the cellchat object with the createCellChat function. The data was preprocessed with the identifyOverExpressedGenes, identifyOverExpressedInteractions and projectData functions using the default parameters. The computeCommunProb, filterCommunication (min.cells = 10) and computeCommunProbPathway functions were then used to determine any potential ligand-receptor interactions. Finally, the cell communication network was aggregated using the aggregateNet function.

Trajectory analysis
For inferring the differentiation trajectory of fibroblasts, we employed the Monocle2 package[54] (version 2.9.0). The methodology entailed the following steps: Firstly, the transition from a Seurat object to a CellDataSet object was executed using the importCDS function. Subsequently, the differentialGeneTest function was applied to identify genes suitable for ordering the fibroblasts (ordering genes, qval <0.01). Following this, dimensionality reduction and clustering were performed with the reduceDimension function. Finally, the differentiation trajectory was deduced by applying the orderCells function.

Metabolic functional scoring analysis using scMetabolism
Metabolic activity at the single-cell level was quantified using the scMetabolism package[55] (version 0.2.1). Based on the conventional single-cell transcriptome expression matrix, the VISION algorithm was applied to score the metabolic activity of each fibroblast, culminating in activity scores for fibroblasts across each metabolic pathway. The software comes preloaded with human metabolic gene sets, encompassing 85 KEGG pathways and 82 REACTOME entries, which were orthologously translated to mouse genes for our analysis.

SCENIC analysis
The SCENIC analysis was run using the motifs database for RcisTarget and GRNboost (SCENIC[56] version 1.2.4, which corresponds to RcisTarget version 1.10.0 and AUCell version 1.12.0) with the default parameters. In detail, transcription factor binding motifs overrepresented on a gene list were identified with RcisTarget package. The activity of each group of regulons in each cell was scored by AUCell package (version 1.12.0).

To evaluate the cell type specificity of each predicted regulon, the regulon specificity score which was based on the Jensen-Shannon divergence, a measure of the similarity between two probability distributions was calculated. Specifically, the JSD (Jensen-Shannon divergence) between each vector of binary regulon activity overlaps with the assignment of cells to a specific cell type was calculated. The connection specificity index for all regulons was calculated with the scFunctions (https://github.com/FloWuenne/scFunctions/) package.

Network analysis using STRING
To dissect the functional connectivity of ferroptosis-related differential genes identified in basal cells, we submitted the gene list to the STRING database (version 12.0, https://string-db.org/) with the species parameter specified as *Mus musculus*. Leveraging STRING's default settings, we constructed a network that encompassed active interaction sources, including experimental data, database records, and predicted interactions. The resultant network was visualized within the STRING interface, facilitating the identification of clusters of interacting proteins or genes, which could suggest shared functional pathways or complexes.

RIOM model
C57BL/6 mice were irradiated with a single dose of 18 Gy targeted to the head using an RS2000 X-ray irradiator (Rad Source Systems, Suwanee, GA, USA) with 1.126 Gy/min. During irradiation, mice were immobilized in a customized lead-shielded jig designed to expose only the head. At the designated time points, the tongues were collected. To evaluate the effects of pharmacological intervention on the development and severity of RIOM, mice were randomly assigned to groups receiving either vehicle control or treatments beginning 7 days prior to irradiation and continuing for 9 days post-irradiation. The treatments included intraperitoneal (i.p.) administration of LIP-1 (5 mg/kg; MedChemExpress, HY-12726), spermidine (10 mg/kg; MedChemExpress, HY-B1776), spermine (10 mg/kg; MedChemExpress, HY-B1777), KGF-1 (6.25 mg/kg; MedChemExpress, HY-P70597), DFMO (300 mg/kg; MedChemExpress, HY-B0744), or topical oral application of benzydamine mouthwash (0.15% w/v; TargetMol, T8807) (Supplementary Table 1). Irradiated mice were monitored daily for signs of mucositis. At designated experimental endpoints, mice were euthanized by CO_2 asphyxiation followed by cervical dislocation, and tongues were dissected for subsequent histological and molecular analysis.

Radiation-induced abdominal damage model
Male C57BL/6 mice were randomly assigned to four groups (*n* = 6/group): Control: i.p. injection of 100 μL saline; Radiation-only: i.p. injection of 100 μL saline + abdominal irradiation; Radiation + spermidine: i.p. injection of spermidine (10 mg/kg in saline) + irradiation; Radiation + amifostine: i.p. injection of amifostine (10 mg/kg, MedChemExpress HY-B0639 in saline) + irradiation. Spermidine and amifostine were administered daily via i.p. injection for 3 consecutive days prior to irradiation. All irradiated groups received a single 10 Gy dose

targeted to the abdomen. During irradiation, a 5-mm lead shield protected the head, thorax, and extremities to minimize off-target effects. Post-irradiation, treatments continued daily for 7 days. On day 8, mice were euthanized by CO_2 asphyxiation followed by cervical dislocation. Colon, liver, and lung tissues were harvested, rinsed in ice-cold saline, and fixed in 4% paraformaldehyde (Beyotime Biotechnology, P0099) for 24 h at 4 °C prior to histopathological processing.

Co-culture experiments

Fibroblasts and basal cells were co-cultured using 6-well Transwell® inserts with 0.4-μm pore polycarbonate membranes (Corning, 3412). Three experimental groups were established: basal cell monoculture (both chambers containing basal cells), fibroblast monoculture (both chambers containing fibroblasts), and co-culture (basal cells upper/ fibroblasts lower), with identical total cell densities maintained across all groups.

RNA interference of gene expression

Small interfering RNA (siRNA) targeting SAT1, ACSL4, JunB, HIF-1α, or JunD (sequences listed in Supplementary Table 4) was synthesized by Beijing Tsingke Biotech Co., Ltd. For transfection, siRNAs were diluted to a working concentration of 125 nM in Opti-MEM® Reduced Serum Medium (Gibco, 31985062), then complexed with Lipofectamine™ 2000 (Invitrogen, L3000015). The siRNA-lipid complexes were incubated at room temperature for 20 minutes before addition to cells cultured at 70% confluency. Cells were harvested 48 hours post-transfection for downstream analysis of gene silencing efficiency.

ROS and lipid peroxidation assay

Cells were seeded in 6-well plates 24 hours prior to irradiation, with or without drug pretreatment. Following radiation exposure, fresh medium containing 4 μM CM-H_2DCFDA (Invitrogen, C6827) for ROS detection or 5 μM BODIPY™ 665/676 (Invitrogen, B3932) for lipid peroxidation quantification was added to each well. After 30-minute incubation at 37 °C/5% CO_2, cells were washed twice with PBS. ROS visualization: Cells in glass-bottom dishes were immediately imaged using a confocal microscope (Olympus FV3000). Lipid peroxidation quantification: cells in 6-well plates were trypsinized, resuspended in PBS containing 1% BSA, and analyzed via flow cytometry (BD FACSCelesta).

Iron content analysis

Total cellular iron content was determined by inductively coupled plasma mass spectrometry (ICP-MS). Cells pretreated with or without drugs for 24 hours were irradiated and incubated for an additional 24 hours. Harvested cells were analyzed via ICP-MS under standard operating conditions using an Agilent 7800 ICP-MS system (Agilent Technologies). Analysis was performed with the following instrument parameters: RF power 1550 W; plasma gas flow 15 L/min; nebulizer gas flow 1 L/min; auxiliary gas flow 0.9 L/min; helium gas flow 5 mL/min in the collision cell. Each sample was introduced for 30 seconds with a peristaltic pump speed of 0.5 rps, preceded by a 30-second stabilization period. Data were acquired with an integration time of 0.3 seconds per mass. Instrument control and data processing were performed using MassHunter Workstation Software (version C.01.06). Iron concentrations were quantified against external calibration standards and normalized to total cell count.

Labile ferrous iron (Fe^{2+}) was detected using FerroOrange (Dojindo, F374). Post-irradiation, cells were incubated with 1 μM FerroOrange in serum-free medium for 30 min at 37 °C/5% CO_2. Without washing to prevent probe leakage, Fe^{2+}-specific fluorescence was immediately captured by confocal microscopy (Olympus FV3000).

AAV transduction in vivo

AAV-mediated gene/shRNA delivery to mouse tongues was achieved via single in situ injection of ~2×10^{11} GC/mouse using the following AAV vector: HBAAV2/9-POSTN-mir30-m-Odc1-shRNA1/2/3-ZsGreen (Cat# HH20250501XAZC-AAV01, Hanbio).

Histology

Tissue specimens were fixed in 4% paraformaldehyde for 24 hours, dehydrated through graded ethanol series (70% → 80% → 95% → 100%I → 100%II), and embedded in paraffin. Sections of 4 μm thickness were prepared using a microtome (Leica RM2016). Prior to staining, sections underwent deparaffinization in xylene and rehydration through a descending ethanol gradient (100% → 95% → deionized water).

H&E staining and Masson's trichrome staining were performed according to the manufacturer's protocols. Stained sections were examined under an optical microscope (Leica Microsystems, Wetzlar, Germany) and analyzed using ImageJ software (National Institutes of Health, Bethesda, MD).

For immunofluorescence staining, Antigen retrieval was performed in preheated Tris-EDTA buffer (10 mM Tris, 1 mM EDTA, pH 9.0) using a pressure cooker (Retriever 2100) at 95–98 °C for 15 min. After blocking with 3% BSA (MACS, 1000076) for 1 hour, sections were incubated with primary antibodies (Supplementary Table 3) overnight at 4 °C. After PBS washes, sections were stained with fluorophore-conjugated secondary antibodies and 0.5 μg/mL DAPI (Invitrogen, D1306) for 5 min. Slides were mounted with antifade medium (Beyotime, P0126) and imaged via confocal microscopy (Olympus FV3000) using sequential scanning to eliminate crosstalk.

For immune-histological staining, Endogenous peroxidase was quenched with 3% H_2O_2 for 15 min. After blocking with 3% BSA, primary antibodies (Supplementary Table 3) were applied overnight at 4 °C. Signal was developed using HRP-conjugated secondary antibodies and DAB substrate (Servicebio, G1212) with strict 90-sec incubation to prevent over-staining. Hematoxylin counterstaining (Servicebio, G1004) was limited to 45 sec. Sections were dehydrated in ethanol, cleared in xylene, and mounted with resin.

Analysis was conducted using ImageJ software. The percentage of positive staining was determined by calculating the ratio of stained area to the total area of the tissue of interest within predefined thresholds, counting all pixels below the threshold in the image.

RNA isolation, reverse transcription, and real time PCR

Total RNA was isolated with TRIzol Reagent (Invitrogen, 15596018CN) following the manufacturer's protocol. Reverse transcription was performed with PrimeScript RT Master Mix (Takara, RR036A). The mRNA levels were quantified via real-time PCR using the TB Green Premix Ex Taq II kit (Takara, RR820A) on the ABI Quant Studio 5 Real-Time PCR System. Primer sequences employed for qRT-PCR are listed in Supplementary Table 4. Individual mRNA levels were normalized to β-actin RNA levels for accurate expression quantification.

ChIP−PCR

Cells were seeded 24 hours prior to irradiation. These cells were then fixed with 1% formaldehyde for 10 minutes at room temperature to cross-link protein-DNA complexes, followed by the addition of glycine (final concentration 0.125 M) and incubation for 5 minutes at room temperature to quench the cross-linking reaction. Subsequently, sonication was performed to disrupt the cells and fragment the chromatin to an appropriate length. Following centrifugation at 12,000 × g for 10 minutes at 4 °C to remove debris, the supernatant was immunoprecipitated by adding antibodies specific to the JUND or HIF-1α transcription factor to bind the protein-DNA complexes. Protein A/G magnetic beads (Millipore, IP05) were utilized to capture the immune complexes, and washing was conducted to remove non-specific bindings. Finally, cross-links were reversed to release the DNA, which was then amplified via PCR to detect the target DNA fragments associated with the gene (Supplementary Table 4),

thereby verifying the binding of the protein to specific DNA sequences.

Intestinal permeability assay

Intestinal barrier integrity was assessed using FITC-labeled dextran (Meiluncell, MB12674). Mice were fasted for 4 hours and then administered FITC-dextran (200 mg/kg) by oral gavage. Blood was collected from the tail vein 4 hours later, and serum was obtained by centrifugation. Fluorescence intensity in the serum was measured using a microplate reader (Bio-tek SynergyLX). The concentration of FITC-dextran in each sample was determined from a standard curve.

mRNA stability assay

Basal cells, initially treated with DFMO or spermidine, were exposed to actinomycin D (5 µg/mL, MedChemExpress, HY-17559). RNA was extracted at sequential intervals post-inhibition. The half-life of mRNA was then determined from the time-dependent decline in its abundance, as quantified by RT-qPCR.

Western blot assay

Basal cells and fibroblasts were washed twice with ice-cold PBS and mechanically detached using cell scrapers. Cell pellets were lysed in RIPA buffer (NCM Biotech, WB3100) supplemented with protease/phosphatase inhibitor cocktail (1:100 v/v; Thermo Fisher, 78446) on ice for 30 min. Lysates were centrifuged at $14,000 \times g$ for 25 min at 4 °C to remove debris. Total protein concentration was determined using a BCA assay kit (Thermo Fisher Scientific, 23225). Equal protein amounts (20 µg/lane) were electrophoresed on 10% Tris-glycine gels (Bio-Rad, 4561033) at 80 V (stacking gel) and 120 V (resolving gel). PVDF membranes (Millipore, IPVH00010) were pre-activated by immersion in 100% methanol for 15 seconds. Proteins were transferred to PVDF membranes. The membranes were blocked in 4% skim milk at room temperature for 1 hour. Primary antibodies (Supplementary Table 3) diluted in antibody dilution buffer (NCM, WB100D) were incubated overnight at 4 °C with gentle agitation. After three 10-min TBST washes, membranes were incubated with HRP-conjugated secondary antibodies (Proteintech; 1:5000 in TBST) for 1 h at 25 °C. Signals were developed using enhanced chemiluminescence substrate (Thermo Fisher, 32109) and the bands were visualized accordingly.

Polyamine extraction and measurement

Polyamine levels were quantified using a validated liquid chromatography-tandem mass spectrometry (LC-MS/MS) method. Briefly, cell or tissue supernatants were derivatized with dansyl chloride (MCE, HY-D0017) to enhance detection sensitivity. Specifically, 100 µL of sample was mixed with 50 µL of 100 mM sodium bicarbonate (Beyotime, ST2650) and 50 µL of dansyl chloride solution (20 mg/mL in acetonitrile), vortexed, and incubated at 60 °C for 20 min in the dark. The reaction was terminated with 50 µL of 1% formic acid (Thermo Fisher Scientific, 28905), and the mixture was centrifuged at 12,000 rpm for 15 min at 4 °C. The supernatant was collected for LC-MS analysis.

Chromatographic separation was performed on an Agilent 1290 system equipped with an Agilent EC-C18 column (3.0 × 50 mm, 2.7 µm) maintained at 40 °C. The mobile phase consisted of (A) 5 mM ammonium formate with 0.1% formic acid in water and (B) acetonitrile, using a gradient elution at a flow rate of 0.4 mL/min: 0–0.2 min, 50% B; 0.2–1 min, 50–95% B; 1–3 min, 95% B; 3–3.5 min, 95% B; 3.5–3.6 min, 95–50% B; 3.6–5 min, 50% B. The injection volume was 5 µL.

Mass spectrometric detection was carried out on an AB SCIEX 3200 QTRAP system with an electrospray ionization source in positive multiple reaction monitoring mode. The ion source temperature was 550 °C, ion spray voltage was 5500 V, and nebulizer (Gas1), turbo (Gas2), curtain, and collision gases were set at 55, 60, 35, and 9 psi, respectively. Optimized parameters for each polyamine were as follows: putrescine (Q1 555.3 → Q3 170.1, DP 115 V, CE 40 V), spermidine (Q1 845.3 → Q3 360.3, DP 180 V, CE 51 V), and spermine (Q1 1135.5 → Q3 360.3, DP 220 V, CE 66 V).

Data acquisition and processing were performed using SCIEX OS software (version 2.0.0.45330) and Analyst® Software (version 1.7.3). Quantification was based on external calibration curves, which exhibited excellent linearity ($R^2 \geq 0.99$) across the measured concentration ranges.

Cell survival assay

Cell proliferation and survival capabilities were assessed using colony formation test, Calcein/PI cell viability and cytotoxicity detection kit (Beyotime, C2015S), and the Cell Counting Kit-8 (CCK-8, Beyotime, C0037).

For colony formation test, basal cells were seeded in a 6-well plate. Twenty-four hours post-seeding, cells were irradiated. Untreated cells received DMSO in their medium, while irradiated cells were treated with medium containing DMSO, 5 µM Ferr-1(MedChemExpress, HY-100579), 5 µM Z-VAD (MedChemExpress, HY-16658B), 2 µM Nec-1s (MedChemExpress, HY-113100), or 5 µM VX-765 (MedChemExpress, HY-13205) (Supplementary Table 2). Culturing medium was changed every other day for a period of 10-14 days. Cells were then fixed in methanol and stained with crystal violet solution (Beyotime, C0121). Colony counts were obtained from three wells per experiment and averaged. Relative survival rates were the ratio of the absolute survival rate (total number of colonies per well) at each radiation dose to the absolute survival rate of unirradiated cells.

For Calcein/PI cell viability and cytotoxicity detection, cells were seeded in a 24-well plate. Twenty-four hours post-seeding, cells were irradiated. After another 24 hours, 250 µL of Calcein AM/PI detection working solution was added to each well and incubated at 37 °C in the dark for 30 minutes. Fluorescence was observed under a fluorescence microscope (Olympus, FV3000), with Calcein AM displaying green fluorescence (Ex/Em = 494/517 nm) and PI showing red fluorescence (Ex/Em = 535/617 nm).

To measure cell viability and proliferation, cells were seeded in a 96-well plate. Medium was supplemented with DMSO or spermine/spermidine (Supplementary Table 2) at concentrations of 10, 20, 30, 40, 50, 60, 70, 80, 90, and 100 nM, or putrescine (MedChemExpress, HY-Y1781) at concentrations of 20, 40, 60, 80, 100, 200, 300, 400, and 500 nM for a 24-hour pre-treatment before radiation. Twenty-four hours post-radiation, 10 µL of CCK-8 solution was added to each well, and cells were incubated for an additional 2-4 hours in the cell culture incubator. Absorbance was measured using a microplate reader (Thermo Scientific) to determine cell viability and proliferation.

TEM observation

Tongue tissues from mice were fixed in 2.5% glutaraldehyde dissolved in phosphate buffer (0.01 M, pH = 7.4). Post-fixation was carried out in 1% osmium tetroxide, followed by dehydration through a graded series of ethanol solutions. The samples were then infiltrated with propylene oxide and embedded in epoxy resin. Ultrathin sections, approximately 90 nanometers thick, were cut and stained with uranyl acetate and lead citrate. Observations were made using a JEM-1230 Transmission Electron Microscope (TEM, JEOL, Tokyo, Japan) operated at 110 kV, providing ultrastructural details of the tissue at high resolution.

Statistical analysis

Data from three or four independent experiments are presented as mean values ± standard deviation (SD). Statistical analyses were performed using GraphPad Prism 9.0 (GraphPad Software, San Diego, CA). Normal distribution of all quantitative measurements was verified. Group differences were assessed using Student's t-tests, One-way ANOVA, and Two-way ANOVA, with Tukey's multiple comparisons test as the post hoc procedure where applicable. To ensure the validity of

the observations, quantitative experiments were replicated at least three times. These criteria provided a rigorous framework for interpreting the results and drawing conclusions based on the data obtained from the experimental replicates.

Reporting summary

Further information on research design is available in the Nature Portfolio Reporting Summary linked to this article.

Data availability

The single-cell RNA sequencing data generated in this study have been deposited in the NCBI Sequence Read Archive (SRA) database under accession codes SRR32273201, SRR32273200 and SRR32305640. All other data supporting the findings from this study are available within the Article and Supplementary information.

References

1. Morral, C. et al. p53 promotes revival stem cells in the regenerating intestine after severe radiation injury. *Nat Commun* **15**, 3018 (2024).
2. Dasgupta, Q. et al. A human lung alveolus-on-a-chip model of acute radiation-induced lung injury. *Nat Commun* **14**, 6506 (2023).
3. Elad, S., Yarom, N., Zadik, Y., Kuten-Shorrer, M. & Sonis, S. T. The broadening scope of oral mucositis and oral ulcerative mucosal toxicities of anticancer therapies. *CA Cancer J Clin* **72**, 57–77 (2022).
4. Sonis, S. T. The pathobiology of mucositis. *Nat. Rev. Cancer.* **4**, 277–284 (2004).
5. Spielberger, R. et al. Palifermin for oral mucositis after intensive therapy for hematologic cancers. *N. Engl. J. Med.* **351**, 2590–2598 (2004).
6. Bian, L., Han, G., Zhao, C. W., Garl, P. J. & Wang, X. J. The role of Smad7 in oral mucositis. *Protein Cell* **6**, 160–169 (2015).
7. Guan, Z. et al. Efficacy of mesenchymal stem cell therapy in rodent models of radiation-induced xerostomia and oral mucositis: a systematic review. *Stem Cell Res Ther* **14**, 82 (2023).
8. Pei, Z. et al. Inhibition of ferroptosis and iron accumulation alleviates pulmonary fibrosis in a bleomycin model. *Redox Biol* **57**, 102509 (2022).
9. Pan, Y. et al. Ferroptotic MSCs protect mice against sepsis via promoting macrophage efferocytosis. *Cell Death Dis* **13**, 825 (2022).
10. Zilka, O. et al. On the mechanism of cytoprotection by ferrostatin-1 and liproxstatin-1 and the role of lipid peroxidation in ferroptotic cell death. *ACS Cent Sci* **3**, 232–243 (2017).
11. Du, Y. & Guo, Z. Recent progress in ferroptosis: inducers and inhibitors. *Cell Death Discov* **8**, 501 (2022).
12. Jiang, X., Stockwell, B. R. & Conrad, M. Ferroptosis: mechanisms, biology and role in disease. *Nat Rev Mol Cell Biol* **22**, 266–282 (2021).
13. Williams, D. W. et al. Human oral mucosa cell atlas reveals a stromal-neutrophil axis regulating tissue immunity. *Cell* **184**, 4090–4104.e15 (2021).
14. Zhang, H. L. et al. PKCβII phosphorylates ACSL4 to amplify lipid peroxidation to induce ferroptosis. *Nat Cell Biol* **24**, 88–98 (2022).
15. Chen, X., Kang, R., Kroemer, G. & Tang, D. Broadening horizons: the role of ferroptosis in cancer. *Nat Rev Clin Oncol* **18**, 280–296 (2021).
16. Kaiko, G. E. et al. The Colonic Crypt Protects Stem Cells from Microbiota-Derived Metabolites. *Cell* **165**, 1708–1720 (2016).
17. Konieczny, P. et al. Interleukin-17 governs hypoxic adaptation of injured epithelium. *Science* **377**, eabg9302 (2022).
18. Ou, Y., Wang, S. J., Li, D., Chu, B. & Gu, W. Activation of SAT1 engages polyamine metabolism with p53-mediated ferroptotic responses. *Proc Natl Acad Sci USA* **113**, E6806–E6812 (2016).
19. Wan, K. et al. Electroacupuncture alleviates neuropathic pain by suppressing ferroptosis in dorsal root ganglion via SAT1/ALOX15 signaling. *Mol Neurobiol* **60**, 6121–6132 (2023).
20. Murthy, D. et al. Cancer-associated fibroblast-derived acetate promotes pancreatic cancer development by altering polyamine metabolism via the ACSS2–SP1–SAT1 axis. *Nat Cell Biol* **26**, 613–627 (2024).
21. Fritsch, S. D. et al. Metabolic support by macrophages sustains colonic epithelial homeostasis. *Cell Metab* **35**, 1931–1943.e8 (2023).
22. Zhao, C. et al. Polyamine metabolism controls B-to-Z DNA transition to orchestrate DNA sensor cGAS activity. *Immunity* **56**, 2508–2522.e6 (2023).
23. Puleston, D. J. et al. Polyamine metabolism is a central determinant of helper T cell lineage fidelity. *Cell* **184**, 4186–4202.e20 (2021).
24. Ji, G. et al. Polyamine Anabolism Promotes Chemotherapy-Induced Breast Cancer Stem Cell Enrichment. *Adv Sci (Weinh)* **11**, e2404853 (2024).
25. Choi, Y. et al. Transcriptional profiling uncovers microglial HIF-1α signaling as a therapeutic target of radiation-induced brain injury. *Free Radic Biol Med.* **239**, 552–564 (2025).
26. Li, L. et al. JunD stabilization results in inhibition of normal intestinal epithelial cell growth through P21 after polyamine depletion. *Gastroenterology* **123**, 764–779 (2002).
27. Li, H. et al. YAP/TAZ drives cell proliferation and tumour growth via a polyamine-eIF5A hypusination-LSD1 axis. *Nat Cell Biol* **24**, 373–383 (2022).
28. Hasenfuss, S. C. et al. Regulation of steatohepatitis and PPARγ signaling by distinct AP-1 dimers. *Cell Metab* **19**, 84–95 (2014).
29. Han, G. et al. Preventive and therapeutic effects of Smad7 on radiation-induced oral mucositis. *Nat Med.* **19**, 421–428 (2013).
30. Stockwell, B. R. et al. Ferroptosis: a regulated cell death nexus linking metabolism, redox biology, and disease. *Cell* **171**, 273–285 (2017).
31. Dixon, S. J. et al. Ferroptosis: an iron-dependent form of non-apoptotic cell death. *Cell* **149**, 1060–1072 (2012).
32. Zheng, C. et al. A noncanonical role of SAT1 enables anchorage independence and peritoneal metastasis in ovarian cancer. *Nat Commun* **16**, 3174 (2025).
33. Li, H. et al. CRISPR/Cas9 Screens Reveal that Hexokinase 2 Enhances Cancer Stemness and Tumorigenicity by Activating the ACSL4-Fatty Acid β-Oxidation Pathway. *Adv Sci (Weinh)* **9**, e2105126 (2022).
34. Co, H. K. C., Wu, C. C., Lee, Y. C. & Chen, S. H. Emergence of large-scale cell death through ferroptotic trigger waves. *Nature* **631**, 654–662 (2024).
35. Riegman, M. et al. Ferroptosis occurs through an osmotic mechanism and propagates independently of cell rupture. *Nat Cell Biol* **22**, 1042–1048 (2020).
36. Pulito, C. et al. Oral mucositis: the hidden side of cancer therapy. *J Exp Clin Cancer Res.* **39**, 210 (2020).
37. Peng, X. et al. Streptococcus salivarius K12 Alleviates Oral Mucositis in Patients Undergoing Radiotherapy for Malignant Head and Neck Tumors: A Randomized Controlled Trial. *J Clin Oncol* **42**, 1426–1435 (2024).
38. Mehraein-Ghomi, F. et al. Androgen receptor requires JunD as a coactivator to switch on an oxidative stress generation pathway in prostate cancer cells. *Cancer Res* **70**, 4560–4568 (2010).
39. Chen, X. et al. Broadening horizons: the role of ferroptosis in cancer. *Nat Rev Clin Oncol* **18**, 280–296 (2021).
40. Bi, G. et al. Polyamine-mediated ferroptosis amplification acts as a targetable vulnerability in cancer. *Nat Commun* **15**, 2461 (2024).
41. Zhang, T. et al. Polyamine pathway activity promotes cysteine essentiality in cancer cells. *Nat Metab* **2**, 1062–1076 (2020).
42. Han, X. et al. Activation of polyamine catabolism promotes glutamine metabolism and creates a targetable vulnerability in lung cancer. *Proc Natl Acad Sci USA* **121**, e2319429121 (2024).
43. Hofer, S. J. et al. Mechanisms of spermidine-induced autophagy and geroprotection. *Nat Aging* **2**, 1112–1129 (2022).

44. Zhang, Y. et al. Polyamine metabolite spermidine rejuvenates oocyte quality by enhancing mitophagy during female reproductive aging. *Nat Aging* **3**, 1372–1386 (2023).

45. Thakur, V. S. et al. Spermidine/spermine N1-acetyltransferase 1 is a gene-specific transcriptional regulator that drives brain tumor aggressiveness. *Oncogene* **38**, 6794–6800 (2019).

46. Pegg, A. E. Spermidine/spermine-N (1)-acetyltransferase: a key metabolic regulator. *Am J Physiol Endocrinol Metab* **294**, E995–E1010 (2008).

47. Youssef, M. A. M. et al. Synergistic effect of spermidine and ciprofloxacin against Alzheimer's disease in male rat via ferroptosis modulation. *Int J Biol Macromol* **263**, 130387 (2024).

48. Van et al. ATP13A2 deficiency disrupts lysosomal polyamine export. *Nature* **578**, 419–424 (2020).

49. Bakiri, L., Lallemand, D., Bossy-Wetzel, E. & Yaniv, M. Cell cycle-dependent variations in c-Jun and JunB phosphorylation: a role in the control of cyclin D1 expression. *EMBO J* **19**, 2056–2068 (2000).

50. Hofer, S. J. et al. Spermidine is essential for fasting-mediated autophagy and longevity. *Nat Cell Biol* **26**, 1571–1584 (2024).

51. Hao, Y. et al. Integrated analysis of multimodal single-cell data. *Cell* **184**, 3573–3587.e29 (2021).

52. Hänzelmann, S., Castelo, R. & Guinney, J. GSVA: gene set variation analysis for microarray and RNA-Seq data. *BMC Bioinformatics* **14**, 7 (2013).

53. Jin, S. et al. Inference and analysis of cell-cell communication using CellChat. *Nat Commun* **12**, 1088 (2021).

54. Trapnell, C. et al. The dynamics and regulators of cell fate decisions are revealed by pseudotemporal ordering of single cells. *Nat Biotechnol* **32**, 381–386 (2014).

55. Wu, Y. et al. Spatiotemporal immune landscape of colorectal cancer liver metastasis at single-cell level. *Cancer Discov* **12**, 134–153 (2022).

56. Aibar, S. et al. SCENIC: single-cell regulatory network inference and clustering. *Nat Methods* **14**, 1083–1086 (2017).

Acknowledgements

Author contributions

W.Y., K.J., K.W., X.L., Y.M., and L.N. designed and organized experiments. W.Y., K.W., X.L., and X.H. performed experiments and analyzed data. W.Y., K.J., K.W., X.L., Qianqian W., M.W., J.W., F.T., and L.N. prepared figures and edited manuscript. W.Y., Qianqian W., X.L., J.W., Q.L., M.S., and L.N. wrote the paper. W.Y., K.J., K.W., X. L., Wen Q., C.A., and L.N. reviewed and revised the paper. L.N. conceived, supervised, and directed the study.

Competing interests

The authors declare no competing interests.

Additional information

Supplementary information The online version contains supplementary material available at https://doi.org/10.1038/s41467-025-67214-5.

Correspondence and requests for materials should be addressed to Lina Niu.

Peer review information *Nature Communications* thanks Omer Yilmaz, and the other, anonymous, reviewer(s) for their contribution to the peer review of this work. A peer review file is available.

Reprints and permissions information is available at http://www.nature.com/reprints

Publisher's note Springer Nature remains neutral with regard to jurisdictional claims in published maps and institutional affiliations.